Advanced Electronic Materials

High-performance Flexible Broadband Photodetectors Based on 2D Hafnium Selenosulfide Nanosheets

--Manuscript Draft--

Manuscript Number:	aelm.201900794R1
Full Title:	High-performance Flexible Broadband Photodetectors Based on 2D Hafnium Selenosulfide Nanosheets
Article Type:	Full Paper
Section/Category:	
Keywords:	Crystal growth; Transition metal dichalcogenides; Photoresponsivity; Specific detectivity; Flexible optoelectronics
Corresponding Author:	Rajesh Kumar Ulaganathan National Taiwan University TAIWAN
Corresponding Author Secondary Information:	
Corresponding Author's Institution:	National Taiwan University
Corresponding Author's Secondary Institution:	
First Author:	Rajesh Kumar Ulaganathan
First Author Secondary Information:	
Order of Authors:	Rajesh Kumar Ulaganathan
	Raman Sankar
	Chang-Yu Lin
	Raghavan Chinnambedu Murugesan
	Kechao Tang
	Fang-Cheng Chou
Order of Authors Secondary Information:	
Abstract:	2D Transition-metal dichalcogenides (TMDC) have attracted significant interest in recent years due to its multiple degrees of freedom on tuning the physical properties via band engineering and dimensionality adjustment. We report the study of ternary 2D hafnium selenosulfide HfSSe (HSS) high-quality single crystals grown with the chemical vapor transport (CVT) technique. The as-grown HSS single crystal exhibits excellent phototransistor performance from the visible to the near-infrared (NIR) spectral range with outstanding stability. A giant photoresponsivity (~6.4×104 A/W at 488 nm) and high specific detectivity (~1014 Jones) were obtained from the device fabricated with exfoliating single crystal HSS of nano-thickness on a rigid Si/SiO2 substrate. The application of HSS single crystal is extended to yield a sensible flexible photodetector of photoresponsivity up to ~1.3 A/W at 980 nm. The photoresponsivity of CVT grown HSS single crystal is significantly larger than those fabricated with other existing Hf-based chalcogenides. Our results suggest that the layered multi-elemental 2D chalcogenide single crystals hold great promise for future wearable electronics and integrated optoelectronic circuits. Keywords: Crystal growth, Transition metal dichalcogenides, Photoresponsivity, Specific detectivity, Flexible optoelectronics
Additional Information:	
Question	**Response**
Please submit a plain text version of your cover letter here.	

	Dr. Hakim Meskine Editor-in-Chief Advanced Electronic Materials Dear Dr. Meskine, Thank you very much for your e-mail dated September 04, 2019, informing us of the reviewers' comments on our manuscript (Full Paper, No. aelm.201900794), entitled "High-performance Flexible Broadband Photodetectors Based on 2D Hafnium Selenosulfide Nanosheets" We are very grateful for the reviewers' constructive comments. In the "Response to Reviewers' Comments", we made our elaborations and revisions (in black color) in response to the reviewers' questions and suggestions (in blue color). To make our responses specific, we have answered the reviewers' questions point by point in the "Response to Reviewers Comments" and highlighted the changes in the revised manuscript and supporting information. We hope that you will now find the work suitable for publication in your prestigious journal. Finally, we want to take this opportunity to thank the reviewers for their helpful comments and suggestions and thank you for considering this paper. Best Regards, Rajesh Kumar Ulaganathan Ph.D. Senior Post-Doctoral Researcher National Taiwan University
Do you or any of your co-authors have a conflict of interest to declare?	No. The authors declare no conflict of interest.

High-performance Flexible Broadband Photodetectors Based on 2D Hafnium Selenosulfide Nanosheets

Rajesh Kumar Ulaganathan, Raman Sankar, Chang-Yu Lin*, Raghavan Chinnambedu Murugesan, Kechao Tang, and Fang-Cheng Chou**

Dr. R. K. Ulaganathan, Prof. R. Sankar, Prof. F. C. Chou
Center for Condensed Matter Sciences
National Taiwan University
Taipei 10617, Taiwan
sankarraman@phys.sinica.edu.tw, fcchou@ntu.edu.tw

Prof. C.-Y Lin
Department of Mechanical Engineering
Chung Yuan Christian University
Taoyuan 32023, Taiwan
cylin@cycu.edu.tw

Prof. C.-Y Lin, Dr. K. Tang
Department of Materials Science and Engineering,
University of California, Berkeley, 94720, USA

Prof. C.-Y Lin, Dr. K. Tang,
Lawrence Berkeley National Laboratory
Materials Sciences Division
Berkeley, USA

Dr. R. C. Murugesan
Aston Institute of Photonic Technologies
Aston University
Birmingham, B4 7ET, UK

Prof. R. Sankar
Institute of Physics
Academia Sinica
Taipei 11529, Taiwan

Prof. F. C. Chou
Taiwan Consortium of Emergent Crystalline Materials
Ministry of Science and Technology
Taipei 10622, Taiwan

Prof. F. C. Chou
Center of Atomic Initiative for New Materials
National Taiwan University
Taipei 10617, Taiwan

Abstract

2D Transition-metal dichalcogenides (TMDC) have attracted significant interest in recent years due to its multiple degrees of freedom on tuning the physical properties via band engineering and dimensionality adjustment. We report the study of ternary 2D hafnium selenosulfide HfSSe (HSS) high-quality single crystals grown with the chemical vapor transport (CVT) technique. The as-grown HSS single crystal exhibits excellent phototransistor performance from the visible to the near-infrared (NIR) spectral range with outstanding stability. A giant photoresponsivity (~6.4×10^4 A/W at 488 nm) and high specific detectivity (~10^{14} Jones) were obtained from the device fabricated with exfoliating single crystal HSS of nano-thickness on a rigid Si/SiO_2 substrate. The application of HSS single crystal is extended to yield a sensible flexible photodetector of photoresponsivity up to ~1.3 A/W at 980 nm. The photoresponsivity of CVT grown HSS single crystal is significantly larger than those fabricated with other existing Hf-based chalcogenides. Our results suggest that the layered multi-elemental 2D chalcogenide single crystals hold great promise for future wearable electronics and integrated optoelectronic circuits.

Keywords: Crystal growth, Transition metal dichalcogenides, Photoresponsivity, Specific detectivity, Flexible optoelectronics

1. Introduction

Photodetectors with broadband detection are highly crucial in civil, military and astronomy fields.[1,2] A wide variety of photodetectors made with narrow band gap semiconductors have been reported.[3,4] However, such photodetectors are still limited in practical application due to lack of broadband absorption and slow response. Layered two-dimensional (2D) materials of nano-thickness have been shown to possess good optoelectronic characteristics leading to great potential on overcoming the major obstacles of effective broadband and sensitivity.[5,6] For example, graphene as the first reported 2D material, has drawn much attention due to its unique electrical and mechanical properties.[7,8] However, graphene exhibits major limitations on the optoelectronic application, such as the weak light absorbance, large dark current, and fast carrier recombination due to zero bandgap.[9,10] There are many alternative layered 2D materials have been tested and reported since, including transition-metal dichalcogenides (TMDC),[11-15] indium selenide (InSe)[16], hexagonal boron nitride (h-BN)[17], and black phosphorus[18]. In the class of layered 2D materials, TMDC holds great promise because of their direct band gap, strong absorption, and atomic-scale thickness with favorable electronic and mechanical properties.

Hafnium (Hf) based chalcogenides have attracted great attention lately due to its intriguing electronic and optical properties[19,20], particularly for the high mobility (1800 to 3500 $cm^2V^{-1}S^{-1}$) and large absorption spectral range (1-2 eV). There are a few reports on the study of photoelectronic properties of HfS_2 and $HfSe_2$,[21-25] but these dichalcogenides are less efficient on broadband photodetection. Comparing to the end compounds of binary HfS_2-$HfSe_2$, the $Hf(S_xSe_{1-x})_2$ alloy show extra degrees of freedom on tailoring the band gaps,[26,27] which is promising for rapid photoresponse in broadband detection. Very recently, 2D layered $Hf(S_xSe_{1-x})_2$ film was reported being deposited on large area of sapphire substrate through chemical vapor deposition (CVD)

technique, and the optoelectronic properties were tuned significantly by varying the S/Se ratio.[28] Since the $Hf(S_xSe_{1-x})_2$ compound exhibits a van der Waals interaction among adjacent layers of hexagonal symmetry, and S/Se atoms are bonded with Hf atoms in octahedral coordination, the van der Waals interaction among adjacent layers allows easy exfoliation into mono or few layered nanoflakes, which adds additional variables on the tuning of electrical and optoelectronic properties for device fabrication. Although $Hf(S_xSe_{1-x})_2$ compounds attracted great attention on the superior tunable optoelectronic properties, the growth of high-quality single crystals with good crystallinity remains to be a challenge, mostly due to the complexity in attaining homogeneous distribution of chemical constituents in single crystals.[29] Particularly, the incongruent melt and non-volatile nature of the intermetallic element have ruled out the possibility of single crystal growth by the typical solution melt-growth techniques.[30] The chemical vapor transport (CVT) method has been proven to grow single crystals of complex materials of incongruent melt character effectively.[30] For growing complex chalcogenide high-quality single crystals, CVT technique offers the best opportunity through a thermodynamically equilibrated vapor phase chemical reaction in the presence of the appropriate transporting agent.

Herein, we report the growth of high-quality HfSSe (HSS) single crystals by the chemical vapor transport (CVT) method using iodine (I_2) as the transporting agent. The optimized growth recipe and structure characterization for the as-grown HSS single crystals are described. The as-grown crystal was used to fabricate photodetectors showing high-performance photoelectronics to cover the range between near-infrared (NIR) to the visible range. The HSS field effect transistors (FETs) shows *n*-type semiconducting behavior like that of HfS_2 and $HfSe_2$. Significantly enhanced photoresponsivity of ~6.4×10^4 A/W at 488 nm with power 9.2 μW/cm^2 is achieved, which is about 10^5 orders larger than the recently reported $Hf(S_xSe_{1-x})_2$ alloy deposited on the sapphire substrate

with a CVD method.[28] In addition, the HSS-FET holds a high specific detectivity of ~ 10^{14} Jones, which is about one to two orders of magnitude higher than that of $Hf(S_xSe_{1-x})_2$ alloy (10^{12} Jones) fabricated by the CVD method,[28] also comparable to the commercially available silicon-based (10^{13} Jones) and InGaAs-based (10^{12-13} Jones) photodetectors. Moreover, the NIR photodetection is achieved up to photoresponsivity of ~ 4.2 A/W and specific detectivity of ~ 3.4×10^{10} Jones at 980 nm. We have tested the potential of HSS crystal flakes to be a flexible phototransistor using polyethylene terephthalate (PET) substrate, the performance of the device at bent state remains to be satisfactory and comparable to the unbent of InSe-FET.[16] These results observed in HSS single crystal hold great potential for the optoelectronics industry, especially on fabricating devices of high photocurrent generation with broadband and flexible photodetectors.

2. Results and Discussion

a. Crystal growth and characterization

For the growth of HSS single crystals, the stoichiometric amount (molar ratio of 1:1:1) of Hf, S and Se powder mixtures prepared at 850 ^{o}C was used as precursor material. The highly volatile iodine was used as a transporting agent. The precursor material and transporting agent were filled and sealed in an evacuated quartz ampoule for the CVT reaction. The crystal growth experiment was carried out in a horizontal two zone muffle furnace. The ampoule containing precursor's site was aligned at 900 ^{o}C as the source zone and the crystal growth zone was maintained at 800 ^{o}C as the sink zone. The temperature gradient between the source and the sink zones was 2.5 °C/cm. **Figure 1**a illustrates the schematic diagram for the CVT growth processes. More details about the growth can be found in the Experimental section. In the CVT process, the powder precursor of the source material is transported in the gas phase via the transport agent and then deposit at the cold zone following nucleation plus stacking with a preferred orientation upon

separating from the transport agent. After the growth period of two weeks, shiny HSS single crystals deposited at the sink zone of the ampoule was gently harvested. The as-grown high-quality HSS single crystal of size 7 x 6 x 2mm^3 obtained by the CVT reaction is shown in Figure 1b. The crystal structure of HSS single crystal with preferred c-axis orientation is illustrated in Figure 1c, where each tri-atomic layer is composed of edge-shared Hf(S, Se)$_6$ octahedron with weak van der Walls interaction among layers. The inter-layer van der Walls interaction made the mechanical exfoliation into mono or few-layer HSS flakes possible, which is similar to that applied on graphene and other 2D van der Waals materials.[11-18] The crystal structure and phase purity of the as-grown single crystal were analyzed by X-ray diffraction (XRD) study. The XRD pattern of the as-grown HSS crystal (Figure 1d) shows diffraction peaks indicating the cleaved surface has *c*-direction preferred orientation indexed with the (00*l*) planes indexed with space group *P3-m1* of c= 0.615 nm, which indicates an 1T-type HSS of lattice size in between those of $HfSe_2$ and HfS_2.[28] The crystal quality of the as-grown HSS single crystal was further characterized by transmission electron microscopy (TEM), Selected-area electron diffraction (SAED) and high-resolution (HR)-TEM, as shown in Figure 1e and 1f. The clear and bright diffraction spots reveal the high crystallinity of the as-grown HSS single crystal and the nanosheets geometry is clearly observed in the cleaved HSS flakes (inset of Figure 1e). The HR-TEM image shows a regular periodic arrangement of atoms in a hexagonal array, as shown in Figure 1e and 1f for the reciprocal and real space lattice symmetry along the c-direction, respectively. Figure 1g shows the layered nature of HSS single crystal by the field emission-scanning electron microscopy (FE-SEM) on the exfoliated HSS flakes of micron thickness, similar to those observed in $HfS_2$and $HfSe_2$ crystals.[21,24]

The as-grown HSS single crystal was examined by energy dispersive X-ray spectroscopy (EDX) mapping analysis to assess the chemical uniformity (**Figure 2**a & Supporting Information

of Figure S1). The S- and Se-mappings indicated by different colors shown in Figure 2a suggest the S-Se homogeneity is acceptable at the micron size level, which is expected for the original ratio of S:Se=1:1 in the powder source of CVT growth without detectable phase separation in domain forms. To find out the average elemental composition of the as-grown HSS single crystals, electron probe micro analysis (EPMA) were performed on HSS crystal using the average of five points in mm separation (Table 1, Supporting Information). The averaged elemental composition was estimated to be ~ $HfS_{1.1}Se_{0.9}$, i.e., a slightly higher loss of Se but refilled by S atoms during the CVT growth process. Although the as-grown HSS crystal has an S:Se ratio deviated from its precursor of designed 1:1, which reflects the relatively higher vapor pressure of Se in the CVT process and the refilling of Se-vacancy with S is a form of antisite defect. Figure 2b shows the Raman spectra of the as-grown HSS single crystal in comparison with the pure $HfSe_2$ and HfS_2. Four characteristic Raman active modes of E_g (Se-Hf), A_{1g} (Se-Hf), E_g (S-Hf), and A_{1g} (S-Hf) from the pure $HfSe_2$ and HfS_2 are identified at 159 cm^{-1}, 208 cm^{-1}, 260 cm^{-1}, and 324 cm^{-1}, respectively.[28] The Raman spectrum of HSS shows A_{1g} modes corresponding to the pure end compounds but with a slight shift toward the expected average in the middle, which is in agreement with the nature of homogeneous alloy for the as-grown HSS crystal.

b. Optical properties

The optical properties of the HSS single crystal were investigated using UV-VIS-NIR absorption and photoluminescence spectroscopy. The absorption spectrum of HSS single crystal is compared with those of HfS_2 and $HfSe_2$, as shown in **Figure 3**a. Comparing to the absorption spectra of HfS_2 and $HfSe_2$ to be highly specific in the visible and NIR regions, respectively, the optical absorption spectrum of HSS is significantly broadened to cover from the visible to the near-infrared region of 400~850 nm significantly. Based on the calculated band gap sizes of HfS_2 -

$HfSe_2$ solid solution,[31] such broadband tunability of HSS must arise from the overlapped bands of $Hf(S_xSe_{1-x})_2$ on the S-rich side. The photoluminescence (PL) studies were further carried out to confirm the band overlapping, where prominent emission peaks of HfS_2 (~688 nm) and $HfSe_2$ (~886 nm) were clearly observed in the as-grown HSS single crystal (Figure 3b). This broadband HSS crystal can hold feasible applications in the photoelectronic field of phototransistors.

In order to fabricate a phototransistor device, the as-grown high-quality HSS single crystal was exfoliated into few-layer nanoflakes through micromechanical exfoliation using a Scotch tape. The few-layered HSS crystalline nanoflakes were subsequently transferred onto a silicon substrate for electrode deposition. The gold (Au) electrode of thickness ~70 nm with a chromium (Cr) adhesion interlayer of thickness ~5 nm was deposited on the exfoliated HSS crystalline nanoflakes. The fabricated FET device structure based on single crystalline HSS nanoflakes is shown in **Figure 4**a. Atomic force microscopy (AFM) was used to analyze the surface roughness and thickness of exfoliated flakes. The thickness of the exfoliated HSS single crystalline nanoflakes is ~15 nm of smooth exfoliated surface, as shown in Figure S2a-b in the Supporting Information. Following the device fabrication procedure, a series of measurement was carried out at room temperature in the air. The output characteristic curves of the drain current (I_{ds}) versus drain voltage (V_{ds}) for the HSS-FET device were measured by varying the gate voltage from $V_g = 0$ to 80 V in +20 V/step at room temperature, as shown in Figure 4b. The linear I_{ds}-V_{ds} relationship indicates that the HSS metal electrode interface is of Ohmic contact and that the HSS-FET device exhibits a typical *n*-type semiconducting behavior. Mobility of HSS-FET were calculated from the mobility equation of $\mu = L/W(\varepsilon_0\varepsilon_r/d)V_{ds}\ (dI_{ds}/dV_g)$, where L is the channel length, W is the channel width, ε_0 is 8.85 $\times 10^{-12}$ Fm^{-1}, ε_r is 3.9 for SiO_2, d is the thickness of SiO_2 (300 nm), V_{ds} is the drain voltage 1 V and dIds/dVg is the transconductance extracted from the transfer curve (Figure S3 of Supporting

Information). The calculated field effect mobility of HSS-FET device with Au contact is ~ 1.5 $cm^2V^{-1}s^{-1}$, which is close to the values to the HfS_2 (~2.4 $cm^2V^{-1}s^{-1}$)[21] and $HfSe_2$ (0.2-6.5 $cm^2V^{-1}s^{-1}$)[23] based transistors. Figure 4c shows the transfer curve characteristics under dark and white light illumination with a constant V_{ds} of 10 V. The drain current of HSS-FET under illumination (pink) is higher than that of the dark (black), as interpreted by the working principle of HSS-FET illustrated in the inset of Figure 4c. At first, the I_{ds} remains higher when the V_g is greater than the threshold voltage (V_{th}) due to fermi level band shifting in upwards. The measured high current under illumination could be attributed to the more electron-hole pair generation for the valence-to-conduction band transition. These increased electrons and holes can be swept to the source-drain electrodes via the electric field in the channel, which results in significantly enhanced photocurrent.[32,33] The above results clearly reveal the suitability of the HSS-FET device for the photodetector applications. Therefore, we employed our devices for the photodetector application with the lasers having 488 nm and 980 nm wavelengths.

Figure 4d illustrates a schematic diagram of HSS-FET device under 488 nm wavelength laser illumination. Figure 4e shows the I_{ds}-V_{ds} curve for the HSS-FET device being measured with the illumination of wavelength 488nm laser under various power from 0 to 740.0 μW/cm^2. I_{ds} increase significantly with the increase of laser power, which indicates more carries are generated at high power in the channel. The high current of the illuminated HSS phototransistor could be related to the photoelectric effect. The photocurrent (I_{ph}= I_{light}-I_{dark}) is estimated from subtracting the light current (I_{light}) by the dark current (I_{dark}), which is shown increasing sub-linearly with respect to the incident powers (Figure S4 of Supporting Information). We have also calculated the photoresponsivity (R_λ) and specific detectivity (D*) of the HSS phototransistor, which are important factors to appraise the sensitivity of photodetectors. Photoresponsivity (R_λ) is defined

by the photocurrent generated per incident photon as $R_\lambda = I_{ph}/ P_\lambda S$, where I_{ph} is the generated photocurrent, P_λ is the incident photon density, and S is the illuminated area of the device.[34,35] Figure 4f shows the calculated photoresponsivity, which is sub linear with respect to the incident photon. Remarkably, we have achieved giant photoresponsivity of ~6.4×10^4 A/W at 9.2 μW/cm^2 of 488 nm (V_g = 0 V & V_{ds} = 10 V), which is about 10^5 orders magnitude higher than the reported $HfS_{2(1-x)}Se_{2x}$ alloy prepared by the CVD method[28], and also greater than other HfS_2 and $HfSe_2$ based photodetectors[21-24], as compared in Table 2 of the Supporting Information. Specific detectivity is usually calculated with $D^* = (S\cdot\Delta f)^{1/2}/NEP$, where S is the effective area, Δf is the electrical bandwidth of the photodetector, and NEP represents the noise equivalent power. NEP represents the minimum incident power that a device can differentiate the signal from the noise. At low NEP, the above equation can be simplified as $D^* = R_\lambda S^{1/2}/(2eI_{dark})^{1/2}$, where R_λ, S, e, and I_{dark} are photoresponsivity, effective area, elementary charge, and dark current, respectively.[36-38] The right axis of Figure 4f shows the specific detectivity with varying power density. The few layered HSS-FET nanoflakes possesses a high D^* ~ 10^{14} Jones at a power 9.2 μW/cm^2 of 488 nm (V_g = 0 V & V_{ds} = 10 V). The obtained D^* is equivalent to the commercial Si (10^{13} Jones)[39] and InGaAs ($10^{12\text{-}13}$ Jones)[39], and larger than the $HfS_{2(1-x)}Se_{2x}$ alloys (10^{10} Jones)[28] HfS_2 (10^{10} Jones)[21] and $HfSe_2$ (10^{11} Jones)[24] in the literature (Table 2, Supporting Information). 3D matrix plot of HSS-FET device is depicted in Figure S5 of the supporting information, an increase of R_λ is observed by raising the V_{ds} from 0 to 10 V and decreasing power intensity. These results indicate that the active HSS single crystalline nanoflakes are highly efficient for the strong light absorption for more exciton generation and rapid carrier separation.

Apart from photoresponsivity and specific detectivity, it is important to estimate external quantum efficiency (EQE) for the effective implementation of photodetectors for the practical

application. The EQE is the number of electrons detected per incident photon, which is expressed as EQE = R_λ hc/eλ, where R_λ, h, c, e, and λ are photoresponsivity, Planck's constant, light speed, elementary charge, and incident light wavelength, respectively.[40,41] The few-layered HSS-FET possesses a high EQE value of ~10^7 (Figure S6, Supporting Information), which is larger than those reported for the HfS_2 and $HfSe_2$-FETs.[21-24] The obtained high EQE could be attributed to the high R_λ and the existence of trap/defect states in the devices. The trap/defect states are able to capture one type of carriers during the electron-hole creation and allow other carriers to transit between the circuits effectively, which in turn enhances the EQE.[42,43]

The time-resolved photoresponse measurement (I_{ds}-t) were carried out with a 488 nm laser source to study the photocurrent dynamics. The single on-off cycle in **Figure 5**a exhibits a quick rise of I_{ds} current under illumination followed by a sudden fall with a slow relaxation after switching off the laser power. The rising time of the HSS-FET was around 20 ms and the relaxing time was 20 ms for the sudden fall plus the 3 s slow relaxation. The response time of the few-layered HSS-FET shows similar results like those of HfS_2,[21] $HfSe_2$,[22] and several other 2D material-based photodetectors.[11-13,16] The stability of the HSS-FET was further analyzed with pulsed illumination over 300 s at V_{ds} = 1, 2 V and V_g = 0 V. Figure 5b shows the on-off cycle by varying V_{ds}, which indicates the reproducible on-off cycle over a period of 300 s to confirm the device robustness and switching stability. More (I_{ds}-t) measurement results with various V_g are described in Figure S7of the supporting information.

There has been a huge demand for photodetectors that are able to perform in the infrared region. Typically, infrared photodetectors are made by silicon, germanium, and InGaAs based semiconducting materials for the commercial purpose.[44-46] Due to the extended broadband absorption of HSS single crystal, we are motivated to investigate the infrared detection. Figure S8

of the supporting information shows the I_{ds}-V_{ds} curve of HSS-FET with 980 nm laser under varying power intensities of 0, 3.8, 10.2, 21.3, and 29.1 mW/cm^2. The output characteristic curve of HSS-FET shows good photoresponse for the near-infrared wavelength for its increases of I_{ds} at higher power and higher V_{ds}. Based on the results of Figure S8, and the photocurrent with varying incident power characteristic shown in Figure 5c, which reveals a sub-linear increase of photocurrent with respect to the incident power. The responsivity and specific detectivity were determined (Figure 5d) under 980 nm laser with power intensities of 3.8 mW/cm^2 on V_g = 0 V, V_{ds} = 10 V. The calculated values of the responsivity and specific detectivity are 4.2 A/W and D* ~ 3.4×10^{10} Jones, respectively. The obtained values are comparable to those of MoS_2 based photodetectors.[47] The I_{ds}-t and stability measurements were also performed with 980 nm laser and displayed in Figure S9 a & b.

Flexible electronic technology gained immense research interest due to the urgent needs of high performance for devices under mechanical deformation, such as devices in the bending, stretching, and twisting states. These cutting-edge applications in real life demand unique materials for flexible optoelectronic applications. We have examined the flexibility performance of HSS crystalline nanoflakes based device fabricated on the PET substrate under both bent and unbent conditions. A schematic illustration of HSS crystalline nanoflakes on PET substrate is depicted in **Figure 6**a. The same device fabrication procedure used on rigid HSS/Si/SiO_2 has been followed for the flexible HSS/PET fabrication. Figure 6b shows the I_{ds}-V_{ds} output characteristics measured by varying the incident laser powers of 3.3, 9.1, 19.3, and 29.6 mW/cm^2 at a wavelength of 980 nm. The flexible HSS-PET device exhibits a strong photoresponse and sub-linearly increases with laser power and V_{ds}. A detector of good photosensitivity (I_{ph}/I_{dark}) has an ability to distinguish noise from the photocurrent. Therefore, we have calculated I_{ph}/I_{dark} ratio with respect to the

incident powers as shown in Figure 6c, which clearly demonstrates that the HSS crystalline nano flakes have good sensitivity on the flexible substrate even at low incident power. Figure 6d shows the responsivity of flexible HSS photodetector under varying incident power at both flat and bending states. For the incident power of 3.3 mW/cm^2, the responsivity of HSS/PET device is around 1.3 A/W at a flat state and 0.4 A/W at a bending state with bending radius of 1 cm. The reduction of responsivity in a bending state might be attributed to the induced strain, which results in a decrease of electron-hole pair generation efficiency.[48] Moreover, the cracks generated in the metal electrodes during the bending can also reduce the responsivity. Typically, the cracks in the metal electrode create high contact resistant with HSS crystalline nanoflakes, which in turn cause a decrease in photoresponsivity.[49] Although the bending causes reduced responsivity, the infrared photodetector fabricated with few-layered HSS crystalline nanoflakes on the flexible substrate still shows reasonable and workable photoresponsivity for the practical application.

3. Summary

In summary, high-quality 2D layered HSS single crystals for the HfS_2-$HfSe_2$ alloy having S:Se ratio to be near 1.1:0.9 have been grown successfully using the CVT technique. The single crystals grown with this method exhibited high crystallinity and phase purity, resulting in excellent optoelectronic properties. The band engineering of HfS_2-$HfSe_2$ binary alloy with tunable band gaps has been successfully utilized, and the observed broadband response of HSS is explained by the band overlap of S- and Se-rich domains created by the slight S-Se imbalance in the CVT growth. The FET device fabricated by the few-layered HSS nanoflakes reveals exceptional photoresponse with giant photoresponsivity and high specific detectivity under both the visible and visible-blind near infrared region, which is ~10^5 orders magnitude higher than the reported $HfS_{2(1-x)}Se_{2x}$ alloy and also greater than other reported HfS_2 and $HfSe_2$ based photodetectors.

Interestingly, the flexible photodetectors based on this few-layered HSS single crystal also show good photoresponsivity under the flat and bending states up to the curvature of 1 cm. All of the reported photoelectric properties make this class of material be promising optoelectronics for the future.

4. Experimental Section

***Preparation of precursor material*:** For the preparation of precursor material, a stoichiometric amount of elemental Hf, S, and Se powder of molar ratio 1:1:1 were mixed and ground using agate mortar. The HfSSe powder mixture (15 gm) was sealed in an evacuated quartz ampoule with hydrogen gas flame. The sealed quartz ampoule (length=35 cm and ID/OD=1.8/2.0 cm) containing precursor material was treated at 850 ^{o}C for 2 days in a horizontal muffle furnace.

Growth of HSS single crystals: Single crystal of HfSSe has been grown with CVT method using the pre-reacted homogeneous fine powder of HfSSe using iodine as a transport agent. 10 mg of HfSSe mixture with 100 mg of I_2 were transferred into the quartz ampoule (length=35 cm and ID/OD=1.3/1.6 cm). All these preparation procedures were carried out in an argon-filled glove box with water and oxygen level below 1ppm, and then the evacuated quartz ampoule (10^{-5} Torr) was sealed off with hydrogen gas flame. The sealed ampoule containing reaction material was kept in the two-zone horizontal furnace with two different temperature zones set at 900 °C and 800 °C in a temperature gradient of ~2.5 °C/cm. The precursor powder was kept at the 900 °C zone and the other end was maintained at 800 °C. HSS single crystals of size up to 2 mm in diameter of millimetre thickness was obtained after a period of 15 days. The obtained plate-like single crystals are easy to cleave for the exfoliation process.

Mechanical Exfoliation & Device Fabrication: The as-grown HSS single crystal was exfoliated into few-layered nanoflakes by using Scotch tape in the micromechanical exfoliation process. The

exfoliated few-layered nanoflakes were transferred onto the silicon substrate having 300 nm-thick silicon dioxide dielectric layer. A thin-metal grid was used to define the source/drain (S/D) electrodes. Subsequently, a 70 nm of gold (Au) with a 5 nm adhesion interlayer of chromium was deposited on the exfoliated HSS nanoflakes by thermal evaporator under vacuum condition of 10^{-6} Torr. After the device fabrication, a post-annealing at 200 °C in nitrogen was carried out for 30 minutes.

Characterizations: The XRD pattern was obtained with Bruker D2 PHASER (CuKα radiation). The scanning electron microscopy (SEM) (FEI, Nova 200) and the transmission electron microscopy (TEM) (JEOL, JEM-2100F) were used to analyze the morphology and crystallinity of HSS single crystal. Raman spectra were collected by Raman spectrometer (HORIBA, Lab RAM HR). V-770 UV-Visible/NIR spectrophotometer was used to measure the absorption spectrum of HfS_2, $HfSe_2$, and HSS single crystals. The atomic force microscopy (AFM-Veeco-3100) was used to verify the thickness and morphology of HSS. The I_{ds}-V_{ds} curves were measured by source meter (Keithley, 2636A), with the optical system including of He-Ne laser, power meter (Ophir, Nova II) and band pass filters.

Supporting Information

Supporting information is available from the Wiley Online Library or from the author.

Acknowledgments

This work was supported by the Ministry of Science and Technology of Taiwan under grant No. MOST-106-2119-M-002 -035 -MY3, AIMA -108L9008, Academia Sinica grant No. (AS-SS-106-01-1 and NM004) and LEAP Berkeley Program. One of the authors RCM wants to thank the support from the Marie Skłodowska-Curie Individual Fellowship (MOFUS, # 795356).

5. References

[1] L. Su, W. Yang, J. Cai, H. Chen, X. Fang, *Small*, **2017**, *13*, 1701687.
[2] H. Chen, K. Liu, L. Hu, A. A. A.-Ghamdi, X. Fang, *Mater. Today*, **2015**, *18*, 493.
[3] Q. Lin, A. Armin, P. L. Burn, P. Meredith, *Nat. Photonics* **2015**, *9*, 687.
[4] J. H. Song, H. Choi, H. T. Pham, S. Jeong, *Nat. Commun.* **2018**, *9*, 4267.
[5] F. Xia, T. Mueller, Y.-M. Lin, A. V.-Garcia, P. Avouris, *Nat. Nanotechnol.* **2009**, *4*, 839.
[6] C.-H. Liu, Y.-C. Chang, T. B. Norris, Z. Zhong, *Nat. Nanotechnol.* **2014**, *9*, 273.
[7] N. O. Weiss, H. Zhou, L. Liao, Y. Liu, S. Jiang, Y. Huang, X. Duan, *Adv. Mater.* **2012**, *24*, 5782.
[8] B. J. Kim, S.-K. Lee, M. S. Kang, J.-H. Ahn, J. H. Cho, *ACS Nano*, **2012**, *6*, 8646.
[9] R. R. Nair, P. Blake, A. N. Grigorenko, K. S. Novoselov, T. J. Booth, T. Stauber, N. M. R. Peres, A. K. Geim, *Science* **2008**, *320*, 1308.
[10] F. H. L. Koppens, T. Mueller, Ph. Avouris, A. C. Ferrari, M. S. Vitiello, M. Polini, *Nat. Nanotechnol.* **2014**, *9*, 780.
[11] O. L.-Sanchez, D. Lembke, M. Kayci, A. Radenovic, Andras Kis, *Nat. Nanotechnol.* **2013**, *8*, 497.
[12] H. Tan, Y. Fan, Y. Zhou, Q. Chen, W. Xu, J. H. Warner, *ACS Nano* **2016**, *10*, 7866.
[13] E. Zhang, P. Wang, Z. Li, H. Wang, C. Song, C. Huang, Z.-G. Chen, L. Yang, K. Zhang, S. Lu, W. Wang, S. Liu, H. Fang, X. Zhou, H. Yan, J. Zou, X. Wan, P. Zhou, W. Hu, F. Xiu, *ACS Nano*, **2016**, *10*, 8067.
[14] Y.-H Chang, W. Zhang, Y. Zhu, Y. Han, J. Pu, J.-K. Chang, W.-T. Hsu, J.-K. Huang, C.-L. Hsu, M.-H. Chiu, T. Takenobu, H. Li, C.-I Wu, W.-H. Chang, A. T. S. Wee, L.-J. Li, *ACS Nano*, **2016**, *10*, 8067.
[15] C. Yan, C. Gong, P. Wangyang, J. Chu, K. Hu, C. Li, X. Wang, X. Du, T. Zhai, Y. Li, J. Xiong, *Adv. Funct. Mater.* **2018**, *28*, 1803305.
[16] S. R. Tamalampudi, Y.-Y. Lu, R. Kumar U, R. Sankar, C.-D. Liao, K. Moorthy B, C.-H. Cheng, F. C. Chou, Y.-T. Chen, *Nano Lett.* **2014**, *14*, 2800.
[17] H. Liu, J. Meng, X. Zhang, Y. Chen, Z. Yin, D. Wang, Y. Wang, J. You, M. Gao, P. Jin, *Nanoscale* **2018**, *10*, 5559.
[18] X. Chen, X. Lu, B. Deng, O. Sinai, Y. Shao, C. Li, S. Yuan, V. Tran, K. Watanabe, T. Taniguchi, D. Naveh, L. Yang, F. Xia, *Nat. Commun.* **2017**, *8*, 1672.
[19] K. Xu, Y. Huang, B. Chen, Y. Xia. W. Lei, Z. Wang, Q. Wang, F. Wang, L. Yin, J. He, *Small* **2016**, *12*, 3106.
[20] K. E. Aretouli, P. Tsipas, D. Tsoutsou, J. M.-Velasco, E. Xenogiannopoulou, S. A. Giamini, E. Vassalou, N. Kelaidis, A. Dimoulas, *Appl Phys Lett*, **2015**, *106*, 143105.
[21] K. Xu, Z. Wang, F. Wang, Y. Huang, F.Wang, Y. Huang, L. Yin, C. Jiang, J. He, *Adv. Mater.* **2015**, *27*, 7881.
[22] D. Wang, J. Meng, X. Zhang, G. Guo, Z. Yin, H. Liu, L. Cheng, M. Gao, J. You, R. Wang, *Chem. Mater.* **2018**, *30*, 3819.
[23] L. Yin, K. Xu, Y. Wen, Z. Wang, Y. Huang, F. Wang, T. A. Shifa, R. Cheng, H. Ma, J. He *Appl Phys Lett*, **2016**, *109*, 213105.
[24] M. Kang, S. Rathi, I. Lee, L. Li, M. A. Khan, D. Lim, Y. Lee, J. Park, S. J. Yun, D.-H. Youn, C. Jun, G.-H. Kim, *Nanoscale* **2017**, *9*, 1645.

[25] C. Yan, L. Gan, X. Zhou, J. Guo, W. Huang, J. Huang, B. Jin, J. Xiong, T. Zhai, Y. Li, *Adv. Funct. Mater.* **2017**, *27*, 1702918.
[26] L. Li, W. Wang, L. Gan, N. Zhou, X. Zhu, Q. Zhang, H. Li, M. Tian, T. Zhai, *Adv. Funct. Mater.* **2016**, *26*, 8281.
[27] P. Perumal, R. K. Ulaganathan, R. Sankar, Y.-M. Liao, T.-M. Sun, M.-W. Chu, F. C. Chou, Y.-T. Chen, M.-H. Shih, Y.-F. Chen, *Adv. Funct. Mater.* **2016**, *26*, 3630.
[28] D. Wang, X. Zhang, G. Guo, S. Gao, X. Li, J. Meng, Z. Yin, H. Liu, M. Gao, L. Cheng, J. You, R. Wang, *Adv. Mater.* **2018**, *30*, 1803285.
[29] A. Ubaldini, J. Jacimovic, N. Ubrig, E. Giannini, *Cryst. Growth Des.* **2013**, *13*, 4453.
[30] M. Binnewies, R. Glaum, M. Schmidt, P. Schmidt, *Z. Anorg. Allg. Chem.* **2013**, *639*, 219.
[31] C. Gaiser, T. Zandt, A. Krapf, R. Serverin, C. Janowitz, R. Manzke, *Phys. Rev. B* **2004**, *69*, 075205.
[32] W. Ouyang, F. Teng, J.-H. He, X. Fang, *Adv. Funct. Mater.* **2019**, 1807672.
[33] M. Buscema, J. O. Island, D. J. Groenendijk, S. I. Blanter, G. A. Steele, H. S. J. van der Zant, A. C.-Gomez, *Chem. Soc. Rev.* **2015**, *44*, 3691.
[34] C.-H. Yeh, H.-C. Chen, H.-C. Lin,Y.-C. Lin, Z.-Y. Liang, M.-Y. Chou, K. Suenaga, P.-W. Chiu, *ACS Nano* **2019**, *13*, 3269.
[35] N. Huo, G. Konstantatos, *Adv. Mater.* **2018**, *30*, 1801164.
[36] R. B. J. Gedrim, M. Shanmugam, N. Jain, C. A. Durcan, M. T. Murphy, T. M. Murray, R. J. Matyi, R. L. Moore, B. Yu, *ACS Nano,* **2014**, *8*, 514.
[37] P. Hu, L. Wang, M. Yoon, J. Zhang, W. Feng, X. Wang, Z. Wen, J. C. Idrobo, Y. Miyamoto, D. B. Geohegan , K. Xiao, *Nano Lett.* **2013**, *13*, 1649.
[38] G. Su, V. G. Hadjiev, P. E. Loya, J. Zhang, S. Lei, S. Maharjan, P. Dong, P. M. Ajayan, J. Lou, H. Peng, *Nano Lett.* **2015**, *15*, 506.
[39] X. Gong, M. Tong, Y. Xia, W. Cai, J. S. Moon, Y. Cao, G. Yu, C.-L. Shieh, B. Nilsson, A. J. Heeger, *Science*, **2009**, *325*, 1665.
[40] Z. Sun, H. Chang, *ACS Nano* **2014**, *8*, 4133.
[41] R. K. Ulaganathan, Y.-Y. Lu, C.-J. Kuo, S. R. Tamalampudi, R. Sankar, K. M. Boopathi, A. Anand, K. Yadav, R. J. Mathew, C.-R. Liu, F. C. Chou,Y.-T. Chen, *Nanoscale* **2016**, *8*, 2284.
[42] G. Konstantatos, M. Badioli, L. Gaudreau, J. Osmond, M. Bernechea, F. P. G. de Arquer, F. Gatti and F. H. L. Koppens, *Nat. Nanotechnol.* **2012**, *7*, 363.
[43] X. Li, J. E. Carey, J. W. Sickler, M. U. Pralle, C. Palsule and C. J. Vineis, *Opt. Express* **2012**, *20*, 5518.
[44] A. Zhang, H. Kim, J. Cheng, Y.-H. Lo, *Nano Lett.* **2010**, *10*, 2117.
[45] L. Cao, J.-S. Park, P. Fan, B. Clemens, M. L. Brongersma, *Nano Lett.* **2010**, *10*, 1229.
[46] C. L. Tsai, K. Y. Cheng, *Appl. Phys. Lett.* **2007**, *91*, 181105.
[47] W. Deng, Y. Chen, C. You, B. An, B. Liu, S. Li, Y. Zhang, H. Yan, L. Sun, *2D Mater.* **2018**, *5*, 045027.
[48] H. J. Conley, B. Wang, J. I. Ziegler, R. F. Haglund Jr, S. T. Pantelides, K. I. Bolotin, *Nano Lett.* **2013**, *13*, 3626.
[49] G.-H. Lee, Y.-J. Yu, X. Cui, N. Petrone, C.-H. Lee, M. S. Choi, D.-Y. Lee, C. Lee, W. J. Yoo, K. Watanabe, T. Taniguchi, C. Nuckolls, P. Kim, J. Hone, *ACS Nano* **201**3, *7*, 7931.

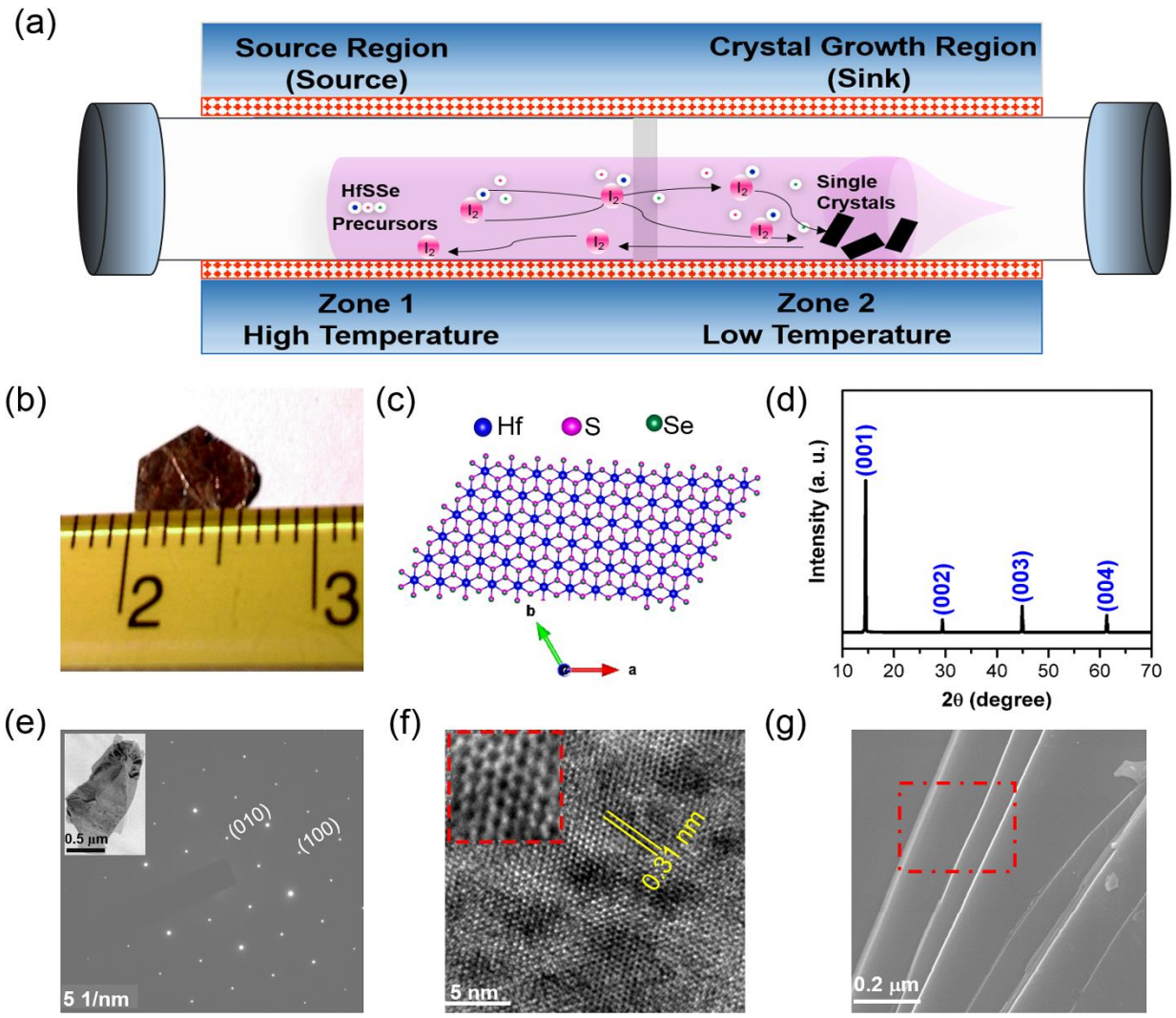

Figure 1. (a) Schematic diagram for CVT method single crystal growth of HSS. (b) Optical image of the as-grown HSS single crystal. (c) Top view of the crystal structure of HSS. (d) XRD diffraction pattern of the as-grown HSS single crystal along the c-direction of preferred orientation. (e) The SAED pattern of HSS crystal, inset shows TEM image of cleaved few-layered HSS flakes, and the corresponding (f) real space view of HSS crystal image through Fourier transform shows a clear hexagonal symmetry with a magnified view in the inset. (g) With the FE-SEM image, clear layered nature is identified for the freshly cleaved HSS single crystal.

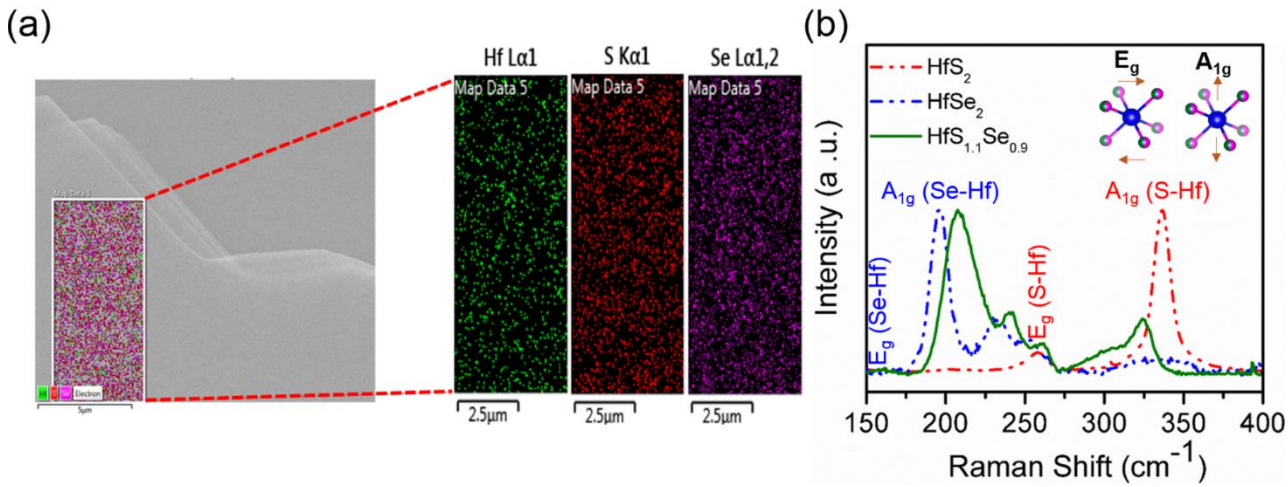

Figure 2. (a) The elemental analysis of the as-grown HSS single crystal, where S and Se mappings display homogeneity at the micron size level. (b) Raman spectra of the HSS flakes measured under ambient conditions with laser excitation at 488 nm. The phonon modes of HSS crystal are compared with the indexed A_{1g} and E_g modes for the pure HfS_2 and $HfSe_2$.

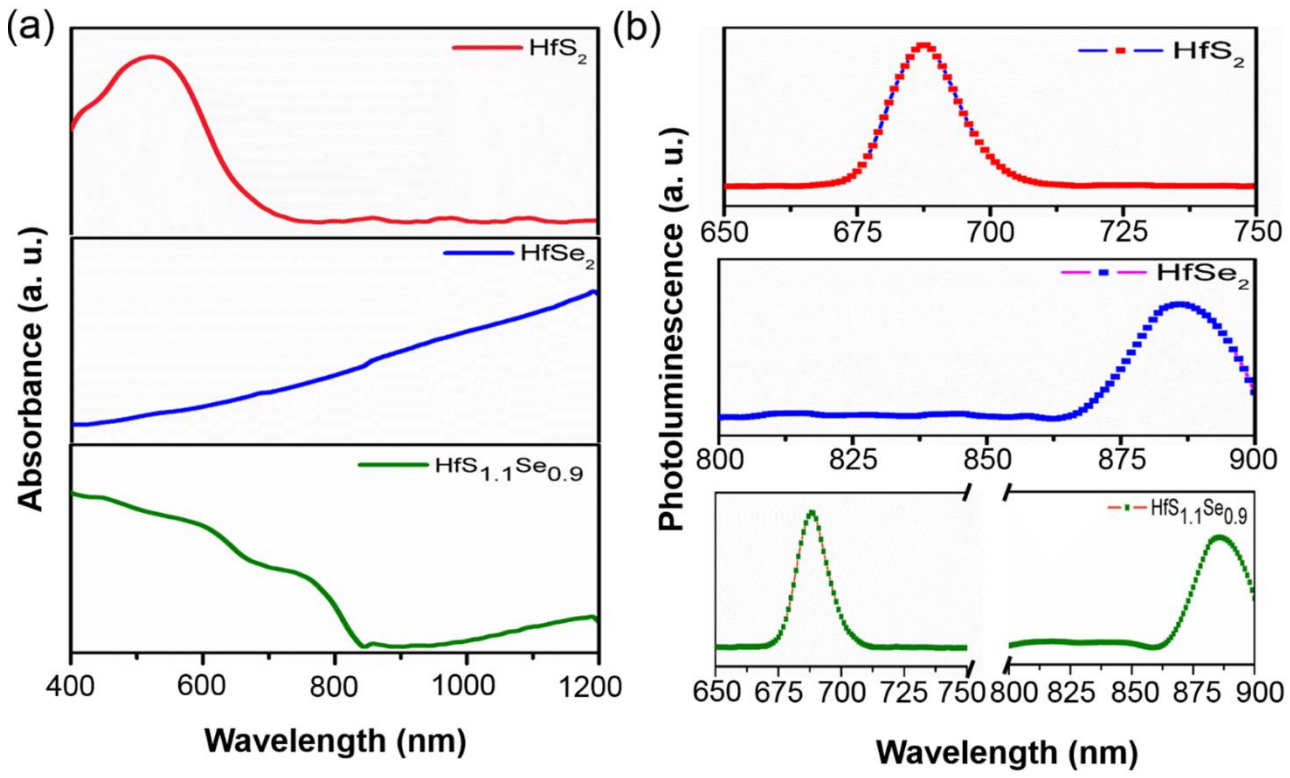

Figure 3. (a) Absorption spectrum of the as-grown $HfS_{1.1}S_{0.9}$ crystal is compared with those of the pristine HfS_2 and $HfSe_2$. (b) Photoluminescence of $HfS_{1.1}S_{0.9}$ shows an emission spectrum at 688 nm and 886 nm, which overlaps with the emission peaks of HfS_2 and $HfSe_2$.

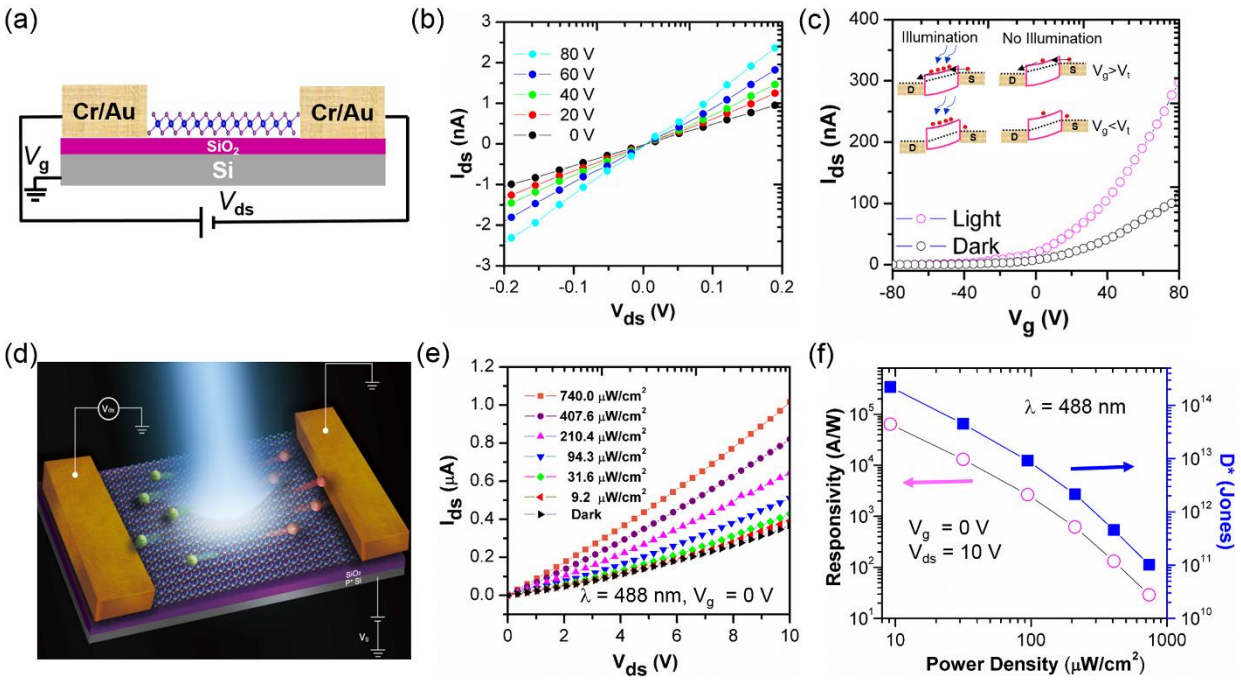

Figure 4. Characteristics of HSS phototransistor prepared on a rigid substrate of SiO_2/Si. (a) The diagrammatic sketch of HSS-FET. (b) Output characteristics of few-layered HSS-FET under different gate voltages from 0 to 80 V in +20 V/step. (c) Transfer characteristics of HSS-FET under dark and white light illumination. Inset shows the band bending diagram under illumination and no illumination with above and below the threshold voltage. (d) The schematic illustration of few-layered HSS under optoelectronic investigation with a laser source. (e) I_{ds}-Vds curve of HSS photodetector in dark and different power of 488 nm laser irradiation. (f) Responsivity and specific detectivity vs power density at 10V of V_{ds} and V_g of 0V.

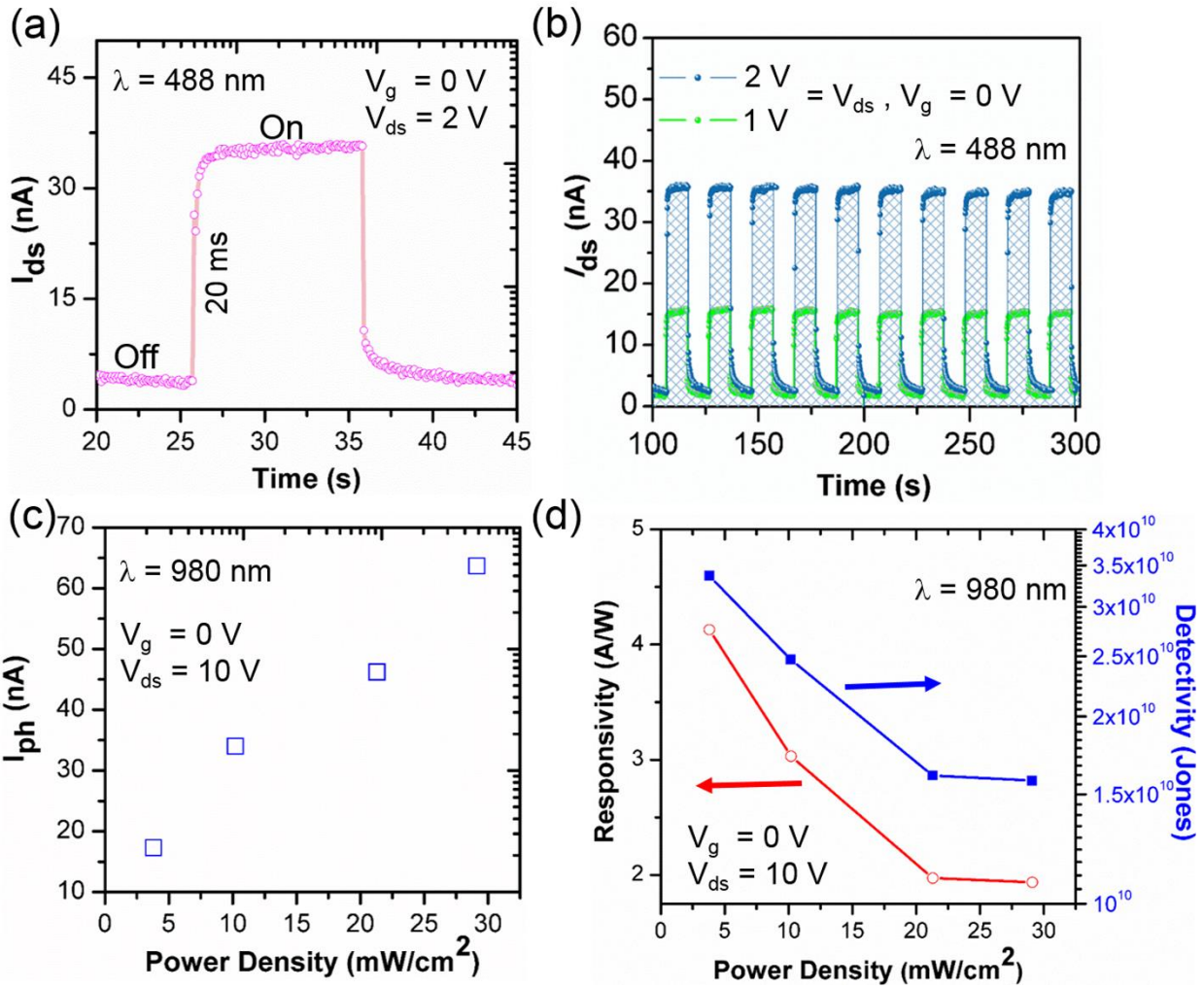

Figure 5. (a)Time-resolved photoresponse of few-layered HSS. (b) Photo switching stability HSS photodetector was examined at various V_{ds} = (1,2), respectively. (c) Infrared-photodetector of few-layered HSS. The Photocurrent (I_{ph}) is plotted as a function of incident laser power. (d) The Responsivity and calculated Detectivity of the HSS were acquired as a function of different incident power of 980 nm.

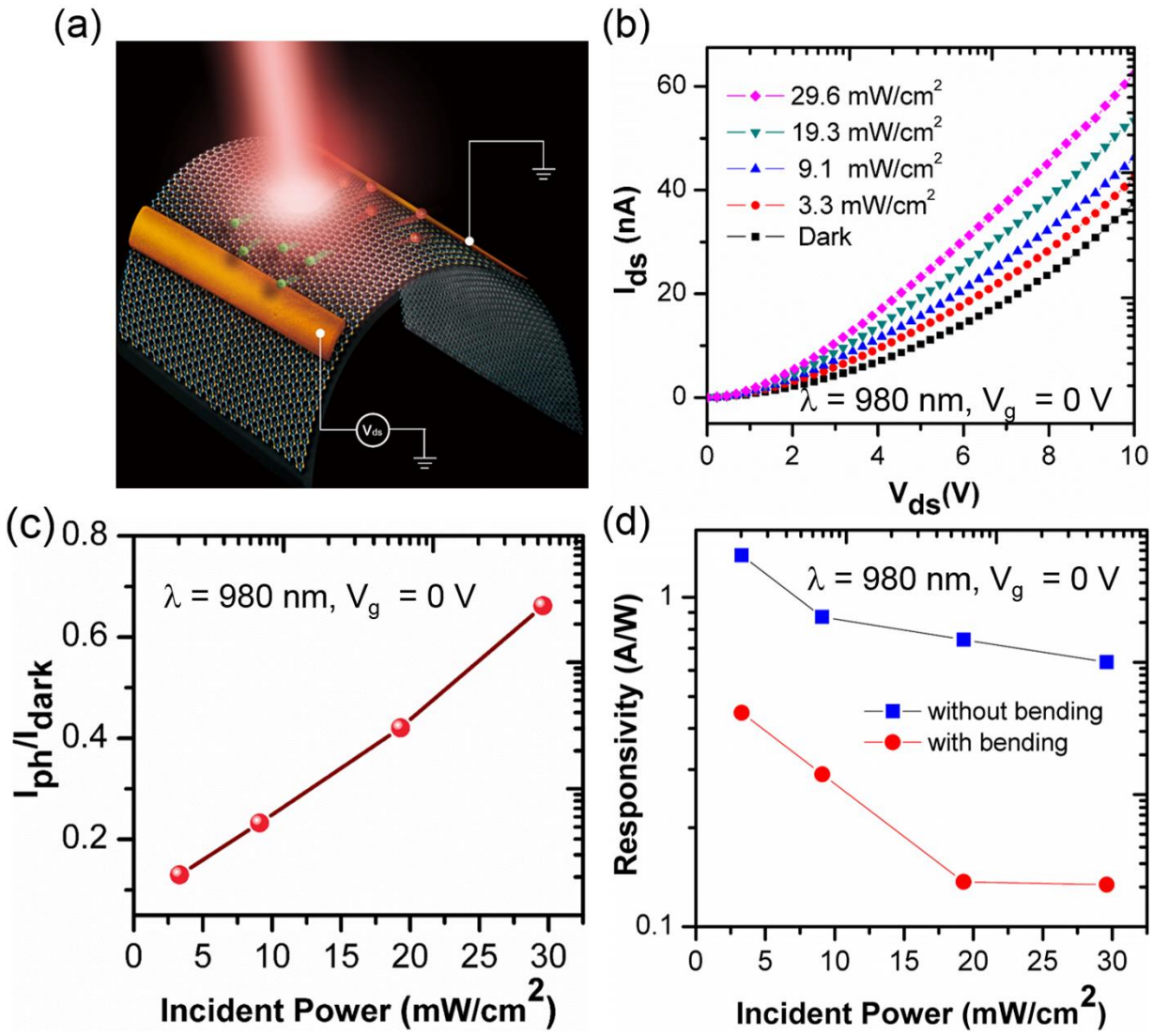

Figure 6. The photodetector of HSS on a flexible PET substrate under 980 nm. (a) Schematic plot of the HSS-FET on a flexible substrate under near-infrared illumination. (b) I_{ds} vs V_{ds} curve under 980 nm irradiation of various power. (c) Photosensitivity (I_{ph}/I_{dark}) measured as a function of incident power density. (d) Responsivity vs. power density under bent with unbent conditions.

High-performance Flexible Broadband Photodetectors Based on 2D Hafnium Selenosulfide Nanosheets

Rajesh Kumar Ulaganathan, Raman Sankar, Chang-Yu Lin*, Raghavan Chinnambedu Murugesan, Kechao Tang, and Fang-Cheng Chou**

Dr. R. K. Ulaganathan, Prof. R. Sankar, Prof. F. C. Chou
Center for Condensed Matter Sciences
National Taiwan University
Taipei 10617, Taiwan
sankarraman@phys.sinica.edu.tw, fcchou@ntu.edu.tw

Prof. C.-Y Lin
Department of Mechanical Engineering
Chung Yuan Christian University
Taoyuan 32023, Taiwan
cylin@cycu.edu.tw

Prof. C.-Y Lin, Dr. K. Tang
Department of Materials Science and Engineering,
University of California, Berkeley, 94720, USA

Prof. C.-Y Lin, Dr. K. Tang,
Lawrence Berkeley National Laboratory
Materials Sciences Division
Berkeley, USA

Dr. R. C. Murugesan
Aston Institute of Photonic Technologies
Aston University
Birmingham, B4 7ET, UK

Prof. R. Sankar
Institute of Physics
Academia Sinica
Taipei 11529, Taiwan

Prof. F. C. Chou
Taiwan Consortium of Emergent Crystalline Materials
Ministry of Science and Technology
Taipei 10622, Taiwan

Prof. F. C. Chou
Center of Atomic Initiative for New Materials
National Taiwan University
Taipei 10617, Taiwan

Abstract

2D Transition-metal dichalcogenides (TMDC) have attracted significant interest in recent years due to its multiple degrees of freedom on tuning the physical properties via band engineering and dimensionality adjustment. We report the study of ternary 2D hafnium selenosulfide HfSSe (HSS) high-quality single crystals grown with the chemical vapor transport (CVT) technique. The as-grown HSS single crystal exhibits excellent phototransistor performance from the visible to the near-infrared (NIR) spectral range with outstanding stability. A giant photoresponsivity (~6.4×10^4 A/W at 488 nm) and high specific detectivity (~10^{14} Jones) were obtained from the device fabricated with exfoliating single crystal HSS of nano-thickness on a rigid Si/SiO_2 substrate. The application of HSS single crystal is extended to yield a sensible flexible photodetector of photoresponsivity up to ~1.3 A/W at 980 nm. The photoresponsivity of CVT grown HSS single crystal is significantly larger than those fabricated with other existing Hf-based chalcogenides. Our results suggest that the layered multi-elemental 2D chalcogenide single crystals hold great promise for future wearable electronics and integrated optoelectronic circuits.

Keywords: Crystal growth, Transition metal dichalcogenides, Photoresponsivity, Specific detectivity, Flexible optoelectronics

1. Introduction

Photodetectors with broadband detection are highly crucial in civil, military and astronomy fields.[1,2] A wide variety of photodetectors made with narrow band gap semiconductors have been reported.[3,4] However, such photodetectors are still limited in practical application due to lack of broadband absorption and slow response. Layered two-dimensional (2D) materials of nano-thickness have been shown to possess good optoelectronic characteristics leading to great potential on overcoming the major obstacles of effective broadband and sensitivity.[5,6] For example, graphene as the first reported 2D material, has drawn much attention due to its unique electrical and mechanical properties.[7,8] However, graphene exhibits major limitations on the optoelectronic application, such as the weak light absorbance, large dark current, and fast carrier recombination due to zero bandgap.[9,10] There are many alternative layered 2D materials have been tested and reported since, including transition-metal dichalcogenides (TMDC),[11-15] indium selenide (InSe)[16], hexagonal boron nitride (h-BN)[17], and black phosphorus[18]. In the class of layered 2D materials, TMDC holds great promise because of their direct band gap, strong absorption, and atomic-scale thickness with favorable electronic and mechanical properties.

Hafnium (Hf) based chalcogenides have attracted great attention lately due to its intriguing electronic and optical properties[19,20], particularly for the high mobility (1800 to 3500 $cm^2V^{-1}S^{-1}$) and large absorption spectral range (1-2 eV). There are a few reports on the study of photoelectronic properties of HfS_2 and $HfSe_2$,[21-25] but these dichalcogenides are less efficient on broadband photodetection. Comparing to the end compounds of binary HfS_2-$HfSe_2$, the $Hf(S_xSe_{1-x})_2$ alloy show extra degrees of freedom on tailoring the band gaps,[26,27] which is promising for rapid photoresponse in broadband detection. Very recently, 2D layered $Hf(S_xSe_{1-x})_2$ film was reported being deposited on large area of sapphire substrate through chemical vapor deposition (CVD)

technique, and the optoelectronic properties were tuned significantly by varying the S/Se ratio.[28] Since the $Hf(S_xSe_{1-x})_2$ compound exhibits a van der Waals interaction among adjacent layers of hexagonal symmetry, and S/Se atoms are bonded with Hf atoms in octahedral coordination, the van der Waals interaction among adjacent layers allows easy exfoliation into mono or few layered nanoflakes, which adds additional variables on the tuning of electrical and optoelectronic properties for device fabrication. Although $Hf(S_xSe_{1-x})_2$ compounds attracted great attention on the superior tunable optoelectronic properties, the growth of high-quality single crystals with good crystallinity remains to be a challenge, mostly due to the complexity in attaining homogeneous distribution of chemical constituents in single crystals.[29] Particularly, the incongruent melt and non-volatile nature of the intermetallic element have ruled out the possibility of single crystal growth by the typical solution melt-growth techniques.[30] The chemical vapor transport (CVT) method has been proven to grow single crystals of complex materials of incongruent melt character effectively.[30] For growing complex chalcogenide high-quality single crystals, CVT technique offers the best opportunity through a thermodynamically equilibrated vapor phase chemical reaction in the presence of the appropriate transporting agent.

Herein, we report the growth of high-quality HfSSe (HSS) single crystals by the chemical vapor transport (CVT) method using iodine (I_2) as the transporting agent. The optimized growth recipe and structure characterization for the as-grown HSS single crystals are described. The as-grown crystal was used to fabricate photodetectors showing high-performance photoelectronics to cover the range between near-infrared (NIR) to the visible range. The HSS field effect transistors (FETs) shows *n*-type semiconducting behavior like that of HfS_2 and $HfSe_2$. Significantly enhanced photoresponsivity of ~6.4×10^4 A/W at 488 nm with power 9.2 μW/cm^2 is achieved, which is about 10^5 orders larger than the recently reported $Hf(S_xSe_{1-x})_2$ alloy deposited on the sapphire substrate

with a CVD method.[28] In addition, the HSS-FET holds a high specific detectivity of ~ 10^{14} Jones, which is about one to two orders of magnitude higher than that of $Hf(S_xSe_{1-x})_2$ alloy (10^{12} Jones) fabricated by the CVD method,[28] also comparable to the commercially available silicon-based (10^{13} Jones) and InGaAs-based (10^{12-13} Jones) photodetectors. Moreover, the NIR photodetection is achieved up to photoresponsivity of ~ 4.2 A/W and specific detectivity of ~ 3.4×10^{10} Jones at 980 nm. We have tested the potential of HSS crystal flakes to be a flexible phototransistor using polyethylene terephthalate (PET) substrate, the performance of the device at bent state remains to be satisfactory and comparable to the unbent of InSe-FET.[16] These results observed in HSS single crystal hold great potential for the optoelectronics industry, especially on fabricating devices of high photocurrent generation with broadband and flexible photodetectors.

2. Results and Discussion

a. Crystal growth and characterization

For the growth of HSS single crystals, the stoichiometric amount (molar ratio of 1:1:1) of Hf, S and Se powder mixtures prepared at 850 ^{o}C was used as precursor material. The highly volatile iodine was used as a transporting agent. The precursor material and transporting agent were filled and sealed in an evacuated quartz ampoule for the CVT reaction. The crystal growth experiment was carried out in a horizontal two zone muffle furnace. The ampoule containing precursor's site was aligned at 900 ^{o}C as the source zone and the crystal growth zone was maintained at 800 ^{o}C as the sink zone. The temperature gradient between the source and the sink zones was 2.5 °C/cm. **Figure 1**a illustrates the schematic diagram for the CVT growth processes. More details about the growth can be found in the Experimental section. In the CVT process, the powder precursor of the source material is transported in the gas phase via the transport agent and then deposit at the cold zone following nucleation plus stacking with a preferred orientation upon

separating from the transport agent. After the growth period of two weeks, shiny HSS single crystals deposited at the sink zone of the ampoule was gently harvested. The as-grown high-quality HSS single crystal of size 7 x 6 x 2mm^3 obtained by the CVT reaction is shown in Figure 1b. The crystal structure of HSS single crystal with preferred c-axis orientation is illustrated in Figure 1c, where each tri-atomic layer is composed of edge-shared Hf(S, Se)$_6$ octahedron with weak van der Walls interaction among layers. The inter-layer van der Walls interaction made the mechanical exfoliation into mono or few-layer HSS flakes possible, which is similar to that applied on graphene and other 2D van der Waals materials.[11-18] The crystal structure and phase purity of the as-grown single crystal were analyzed by X-ray diffraction (XRD) study. The XRD pattern of the as-grown HSS crystal (Figure 1d) shows diffraction peaks indicating the cleaved surface has *c*-direction preferred orientation indexed with the (00*l*) planes indexed with space group *P3-m1* of c= 0.615 nm, which indicates an 1T-type HSS of lattice size in between those of $HfSe_2$ and HfS_2.[28] The crystal quality of the as-grown HSS single crystal was further characterized by transmission electron microscopy (TEM), Selected-area electron diffraction (SAED) and high-resolution (HR)-TEM, as shown in Figure 1e and 1f. The clear and bright diffraction spots reveal the high crystallinity of the as-grown HSS single crystal and the nanosheets geometry is clearly observed in the cleaved HSS flakes (inset of Figure 1e). The HR-TEM image shows a regular periodic arrangement of atoms in a hexagonal array, as shown in Figure 1e and 1f for the reciprocal and real space lattice symmetry along the c-direction, respectively. Figure 1g shows the layered nature of HSS single crystal by the field emission-scanning electron microscopy (FE-SEM) on the exfoliated HSS flakes of micron thickness, similar to those observed in $HfS_2$and $HfSe_2$ crystals.[21,24]

The as-grown HSS single crystal was examined by energy dispersive X-ray spectroscopy (EDX) mapping analysis to assess the chemical uniformity (**Figure 2**a & Supporting Information

of Figure S1). The S- and Se-mappings indicated by different colors shown in Figure 2a suggest the S-Se homogeneity is acceptable at the micron size level, which is expected for the original ratio of S:Se=1:1 in the powder source of CVT growth without detectable phase separation in domain forms. To find out the average elemental composition of the as-grown HSS single crystals, electron probe micro analysis (EPMA) were performed on HSS crystal using the average of five points in mm separation (Table 1, Supporting Information). The averaged elemental composition was estimated to be ~ $HfS_{1.1}Se_{0.9}$, i.e., a slightly higher loss of Se but refilled by S atoms during the CVT growth process. Although the as-grown HSS crystal has an S:Se ratio deviated from its precursor of designed 1:1, which reflects the relatively higher vapor pressure of Se in the CVT process and the refilling of Se-vacancy with S is a form of antisite defect. Figure 2b shows the Raman spectra of the as-grown HSS single crystal in comparison with the pure $HfSe_2$ and HfS_2. Four characteristic Raman active modes of E_g (Se-Hf), A_{1g} (Se-Hf), E_g (S-Hf), and A_{1g} (S-Hf) from the pure $HfSe_2$ and HfS_2 are identified at 159 cm^{-1}, 208 cm^{-1}, 260 cm^{-1}, and 324 cm^{-1}, respectively.[28] The Raman spectrum of HSS shows A_{1g} modes corresponding to the pure end compounds but with a slight shift toward the expected average in the middle, which is in agreement with the nature of homogeneous alloy for the as-grown HSS crystal.

b. Optical properties

The optical properties of the HSS single crystal were investigated using UV-VIS-NIR absorption and photoluminescence spectroscopy. The absorption spectrum of HSS single crystal is compared with those of HfS_2 and $HfSe_2$, as shown in **Figure 3**a. Comparing to the absorption spectra of HfS_2 and $HfSe_2$ to be highly specific in the visible and NIR regions, respectively, the optical absorption spectrum of HSS is significantly broadened to cover from the visible to the near-infrared region of 400~850 nm significantly. Based on the calculated band gap sizes of HfS_2 -

$HfSe_2$ solid solution,[31] such broadband tunability of HSS must arise from the overlapped bands of $Hf(S_xSe_{1-x})_2$ on the S-rich side. The photoluminescence (PL) studies were further carried out to confirm the band overlapping, where prominent emission peaks of HfS_2 (~688 nm) and $HfSe_2$ (~886 nm) were clearly observed in the as-grown HSS single crystal (Figure 3b). This broadband HSS crystal can hold feasible applications in the photoelectronic field of phototransistors.

In order to fabricate a phototransistor device, the as-grown high-quality HSS single crystal was exfoliated into few-layer nanoflakes through micromechanical exfoliation using a Scotch tape. The few-layered HSS crystalline nanoflakes were subsequently transferred onto a silicon substrate for electrode deposition. The gold (Au) electrode of thickness ~70 nm with a chromium (Cr) adhesion interlayer of thickness ~5 nm was deposited on the exfoliated HSS crystalline nanoflakes. The fabricated FET device structure based on single crystalline HSS nanoflakes is shown in **Figure 4**a. Atomic force microscopy (AFM) was used to analyze the surface roughness and thickness of exfoliated flakes. The thickness of the exfoliated HSS single crystalline nanoflakes is ~15 nm of smooth exfoliated surface, as shown in Figure S2a-b in the Supporting Information. Following the device fabrication procedure, a series of measurement was carried out at room temperature in the air. The output characteristic curves of the drain current (I_{ds}) versus drain voltage (V_{ds}) for the HSS-FET device were measured by varying the gate voltage from $V_g = 0$ to 80 V in +20 V/step at room temperature, as shown in Figure 4b. The linear I_{ds}-V_{ds} relationship indicates that the HSS metal electrode interface is of Ohmic contact and that the HSS-FET device exhibits a typical *n*-type semiconducting behavior. Mobility of HSS-FET were calculated from the mobility equation of $\mu = L/W(\varepsilon_0\varepsilon_r/d)V_{ds}\ (dI_{ds}/dV_g)$, where L is the channel length, W is the channel width, ε_0 is 8.85 $\times 10^{-12}$ Fm^{-1}, ε_r is 3.9 for SiO_2, d is the thickness of SiO_2 (300 nm), V_{ds} is the drain voltage 1 V and dIds/dVg is the transconductance extracted from the transfer curve (Figure S3 of Supporting

Information). The calculated field effect mobility of HSS-FET device with Au contact is ~ 1.5 $cm^2V^{-1}s^{-1}$, which is close to the values to the HfS_2 (~2.4 $cm^2V^{-1}s^{-1}$)[21] and $HfSe_2$ (0.2-6.5 $cm^2V^{-1}s^{-1}$)[23] based transistors. Figure 4c shows the transfer curve characteristics under dark and white light illumination with a constant V_{ds} of 10 V. The drain current of HSS-FET under illumination (pink) is higher than that of the dark (black), as interpreted by the working principle of HSS-FET illustrated in the inset of Figure 4c. At first, the I_{ds} remains higher when the V_g is greater than the threshold voltage (V_{th}) due to fermi level band shifting in upwards. The measured high current under illumination could be attributed to the more electron-hole pair generation for the valence-to-conduction band transition. These increased electrons and holes can be swept to the source-drain electrodes via the electric field in the channel, which results in significantly enhanced photocurrent.[32,33] The above results clearly reveal the suitability of the HSS-FET device for the photodetector applications. Therefore, we employed our devices for the photodetector application with the lasers having 488 nm and 980 nm wavelengths.

Figure 4d illustrates a schematic diagram of HSS-FET device under 488 nm wavelength laser illumination. Figure 4e shows the I_{ds}-V_{ds} curve for the HSS-FET device being measured with the illumination of wavelength 488nm laser under various power from 0 to 740.0 μW/cm^2. I_{ds} increase significantly with the increase of laser power, which indicates more carries are generated at high power in the channel. The high current of the illuminated HSS phototransistor could be related to the photoelectric effect. The photocurrent (I_{ph}= I_{light}-I_{dark}) is estimated from subtracting the light current (I_{light}) by the dark current (I_{dark}), which is shown increasing sub-linearly with respect to the incident powers (Figure S4 of Supporting Information). We have also calculated the photoresponsivity (R_λ) and specific detectivity (D*) of the HSS phototransistor, which are important factors to appraise the sensitivity of photodetectors. Photoresponsivity (R_λ) is defined

by the photocurrent generated per incident photon as $R_\lambda = I_{ph}/ P_\lambda S$, where I_{ph} is the generated photocurrent, P_λ is the incident photon density, and S is the illuminated area of the device.[34,35] Figure 4f shows the calculated photoresponsivity, which is sub linear with respect to the incident photon. Remarkably, we have achieved giant photoresponsivity of ~6.4×10^4 A/W at 9.2 μW/cm^2 of 488 nm (V_g = 0 V & V_{ds} = 10 V), which is about 10^5 orders magnitude higher than the reported $HfS_{2(1-x)}Se_{2x}$ alloy prepared by the CVD method[28], and also greater than other HfS_2 and $HfSe_2$ based photodetectors[21-24], as compared in Table 2 of the Supporting Information. Specific detectivity is usually calculated with $D^* = (S\cdot\Delta f)^{1/2}/NEP$, where S is the effective area, Δf is the electrical bandwidth of the photodetector, and NEP represents the noise equivalent power. NEP represents the minimum incident power that a device can differentiate the signal from the noise. At low NEP, the above equation can be simplified as $D^* = R_\lambda S^{1/2}/(2eI_{dark})^{1/2}$, where R_λ, S, e, and I_{dark} are photoresponsivity, effective area, elementary charge, and dark current, respectively.[36-38] The right axis of Figure 4f shows the specific detectivity with varying power density. The few layered HSS-FET nanoflakes possesses a high D^* ~ 10^{14} Jones at a power 9.2 μW/cm^2 of 488 nm (V_g = 0 V & V_{ds} = 10 V). The obtained D^* is equivalent to the commercial Si (10^{13} Jones)[39] and InGaAs ($10^{12\text{-}13}$ Jones)[39] , and larger than the $HfS_{2(1-x)}Se_{2x}$ alloys (10^{10} Jones)[28] HfS_2 (10^{10} Jones)[21] and $HfSe_2$ (10^{11} Jones)[24] in the literature (Table 2, Supporting Information). 3D matrix plot of HSS-FET device is depicted in Figure S5 of the supporting information, an increase of R_λ is observed by raising the V_{ds} from 0 to 10 V and decreasing power intensity. These results indicate that the active HSS single crystalline nanoflakes are highly efficient for the strong light absorption for more exciton generation and rapid carrier separation.

Apart from photoresponsivity and specific detectivity, it is important to estimate external quantum efficiency (EQE) for the effective implementation of photodetectors for the practical

application. The EQE is the number of electrons detected per incident photon, which is expressed as EQE = R_λ hc/eλ, where R_λ, h, c, e, and λ are photoresponsivity, Planck's constant, light speed, elementary charge, and incident light wavelength, respectively.[40,41] The few-layered HSS-FET possesses a high EQE value of ~10^7 (Figure S6, Supporting Information), which is larger than those reported for the HfS_2 and $HfSe_2$-FETs.[21-24] The obtained high EQE could be attributed to the high R_λ and the existence of trap/defect states in the devices. The trap/defect states are able to capture one type of carriers during the electron-hole creation and allow other carriers to transit between the circuits effectively, which in turn enhances the EQE.[42,43]

The time-resolved photoresponse measurement (I_{ds}-t) were carried out with a 488 nm laser source to study the photocurrent dynamics. The single on-off cycle in **Figure 5**a exhibits a quick rise of I_{ds} current under illumination followed by a sudden fall with a slow relaxation after switching off the laser power. The rising time of the HSS-FET was around 20 ms and the relaxing time was 20 ms for the sudden fall plus the 3 s slow relaxation. The response time of the few-layered HSS-FET shows similar results like those of HfS_2,[21] $HfSe_2$,[22] and several other 2D material-based photodetectors.[11-13,16] The stability of the HSS-FET was further analyzed with pulsed illumination over 300 s at V_{ds} = 1, 2 V and V_g = 0 V. Figure 5b shows the on-off cycle by varying V_{ds}, which indicates the reproducible on-off cycle over a period of 300 s to confirm the device robustness and switching stability. More (I_{ds}-t) measurement results with various V_g are described in Figure S7of the supporting information.

There has been a huge demand for photodetectors that are able to perform in the infrared region. Typically, infrared photodetectors are made by silicon, germanium, and InGaAs based semiconducting materials for the commercial purpose.[44-46] Due to the extended broadband absorption of HSS single crystal, we are motivated to investigate the infrared detection. Figure S8

of the supporting information shows the I_{ds}-V_{ds} curve of HSS-FET with 980 nm laser under varying power intensities of 0, 3.8, 10.2, 21.3, and 29.1 mW/cm^2. The output characteristic curve of HSS-FET shows good photoresponse for the near-infrared wavelength for its increases of I_{ds} at higher power and higher V_{ds}. Based on the results of Figure S8, and the photocurrent with varying incident power characteristic shown in Figure 5c, which reveals a sub-linear increase of photocurrent with respect to the incident power. The responsivity and specific detectivity were determined (Figure 5d) under 980 nm laser with power intensities of 3.8 mW/cm^2 on V_g = 0 V, V_{ds} = 10 V. The calculated values of the responsivity and specific detectivity are 4.2 A/W and D* ~ 3.4×10^{10} Jones, respectively. The obtained values are comparable to those of MoS_2 based photodetectors.[47] The I_{ds}-t and stability measurements were also performed with 980 nm laser and displayed in Figure S9 a & b.

Flexible electronic technology gained immense research interest due to the urgent needs of high performance for devices under mechanical deformation, such as devices in the bending, stretching, and twisting states. These cutting-edge applications in real life demand unique materials for flexible optoelectronic applications. We have examined the flexibility performance of HSS crystalline nanoflakes based device fabricated on the PET substrate under both bent and unbent conditions. A schematic illustration of HSS crystalline nanoflakes on PET substrate is depicted in **Figure 6**a. The same device fabrication procedure used on rigid HSS/Si/SiO_2 has been followed for the flexible HSS/PET fabrication. Figure 6b shows the I_{ds}-V_{ds} output characteristics measured by varying the incident laser powers of 3.3, 9.1, 19.3, and 29.6 mW/cm^2 at a wavelength of 980 nm. The flexible HSS-PET device exhibits a strong photoresponse and sub-linearly increases with laser power and V_{ds}. A detector of good photosensitivity (I_{ph}/I_{dark}) has an ability to distinguish noise from the photocurrent. Therefore, we have calculated I_{ph}/I_{dark} ratio with respect to the

incident powers as shown in Figure 6c, which clearly demonstrates that the HSS crystalline nano flakes have good sensitivity on the flexible substrate even at low incident power. Figure 6d shows the responsivity of flexible HSS photodetector under varying incident power at both flat and bending states. For the incident power of 3.3 mW/cm^2, the responsivity of HSS/PET device is around 1.3 A/W at a flat state and 0.4 A/W at a bending state with bending radius of 1 cm. The reduction of responsivity in a bending state might be attributed to the induced strain, which results in a decrease of electron-hole pair generation efficiency.[48] Moreover, the cracks generated in the metal electrodes during the bending can also reduce the responsivity. Typically, the cracks in the metal electrode create high contact resistant with HSS crystalline nanoflakes, which in turn cause a decrease in photoresponsivity.[49] Although the bending causes reduced responsivity, the infrared photodetector fabricated with few-layered HSS crystalline nanoflakes on the flexible substrate still shows reasonable and workable photoresponsivity for the practical application.

3. Summary

In summary, high-quality 2D layered HSS single crystals for the HfS_2-$HfSe_2$ alloy having S:Se ratio to be near 1.1:0.9 have been grown successfully using the CVT technique. The single crystals grown with this method exhibited high crystallinity and phase purity, resulting in excellent optoelectronic properties. The band engineering of HfS_2-$HfSe_2$ binary alloy with tunable band gaps has been successfully utilized, and the observed broadband response of HSS is explained by the band overlap of S- and Se-rich domains created by the slight S-Se imbalance in the CVT growth. The FET device fabricated by the few-layered HSS nanoflakes reveals exceptional photoresponse with giant photoresponsivity and high specific detectivity under both the visible and visible-blind near infrared region, which is ~10^5 orders magnitude higher than the reported $HfS_{2(1-x)}Se_{2x}$ alloy and also greater than other reported HfS_2 and $HfSe_2$ based photodetectors.

Interestingly, the flexible photodetectors based on this few-layered HSS single crystal also show good photoresponsivity under the flat and bending states up to the curvature of 1 cm. All of the reported photoelectric properties make this class of material be promising optoelectronics for the future.

4. Experimental Section

***Preparation of precursor material*:** For the preparation of precursor material, a stoichiometric amount of elemental Hf, S, and Se powder of molar ratio 1:1:1 were mixed and ground using agate mortar. The HfSSe powder mixture (15 gm) was sealed in an evacuated quartz ampoule with hydrogen gas flame. The sealed quartz ampoule (length=35 cm and ID/OD=1.8/2.0 cm) containing precursor material was treated at 850 ^{o}C for 2 days in a horizontal muffle furnace.

Growth of HSS single crystals: Single crystal of HfSSe has been grown with CVT method using the pre-reacted homogeneous fine powder of HfSSe using iodine as a transport agent. 10 mg of HfSSe mixture with 100 mg of I_2 were transferred into the quartz ampoule (length=35 cm and ID/OD=1.3/1.6 cm). All these preparation procedures were carried out in an argon-filled glove box with water and oxygen level below 1ppm, and then the evacuated quartz ampoule (10^{-5} Torr) was sealed off with hydrogen gas flame. The sealed ampoule containing reaction material was kept in the two-zone horizontal furnace with two different temperature zones set at 900 °C and 800 °C in a temperature gradient of ~2.5 °C/cm. The precursor powder was kept at the 900 °C zone and the other end was maintained at 800 °C. HSS single crystals of size up to 2 mm in diameter of millimetre thickness was obtained after a period of 15 days. The obtained plate-like single crystals are easy to cleave for the exfoliation process.

Mechanical Exfoliation & Device Fabrication: The as-grown HSS single crystal was exfoliated into few-layered nanoflakes by using Scotch tape in the micromechanical exfoliation process. The

exfoliated few-layered nanoflakes were transferred onto the silicon substrate having 300 nm-thick silicon dioxide dielectric layer. A thin-metal grid was used to define the source/drain (S/D) electrodes. Subsequently, a 70 nm of gold (Au) with a 5 nm adhesion interlayer of chromium was deposited on the exfoliated HSS nanoflakes by thermal evaporator under vacuum condition of 10^{-6} Torr. After the device fabrication, a post-annealing at 200 °C in nitrogen was carried out for 30 minutes.

Characterizations: The XRD pattern was obtained with Bruker D2 PHASER (CuKα radiation). The scanning electron microscopy (SEM) (FEI, Nova 200) and the transmission electron microscopy (TEM) (JEOL, JEM-2100F) were used to analyze the morphology and crystallinity of HSS single crystal. Raman spectra were collected by Raman spectrometer (HORIBA, Lab RAM HR). V-770 UV-Visible/NIR spectrophotometer was used to measure the absorption spectrum of HfS_2, $HfSe_2$, and HSS single crystals. The atomic force microscopy (AFM-Veeco-3100) was used to verify the thickness and morphology of HSS. The I_{ds}-V_{ds} curves were measured by source meter (Keithley, 2636A), with the optical system including of He-Ne laser, power meter (Ophir, Nova II) and band pass filters.

Supporting Information

Supporting information is available from the Wiley Online Library or from the author.

Acknowledgments

This work was supported by the Ministry of Science and Technology of Taiwan under grant No. MOST-106-2119-M-002 -035 -MY3, AIMA -108L9008, Academia Sinica grant No. (AS-SS-106-01-1 and NM004) and LEAP Berkeley Program. One of the authors RCM wants to thank the support from the Marie Skłodowska-Curie Individual Fellowship (MOFUS, # 795356).

5. References

[1] L. Su, W. Yang, J. Cai, H. Chen, X. Fang, *Small*, **2017**, *13*, 1701687.
[2] H. Chen, K. Liu, L. Hu, A. A. A.-Ghamdi, X. Fang, *Mater. Today*, **2015**, *18*, 493.
[3] Q. Lin, A. Armin, P. L. Burn, P. Meredith, *Nat. Photonics* **2015**, *9*, 687.
[4] J. H. Song, H. Choi, H. T. Pham, S. Jeong, *Nat. Commun.* **2018**, *9*, 4267.
[5] F. Xia, T. Mueller, Y.-M. Lin, A. V.-Garcia, P. Avouris, *Nat. Nanotechnol.* **2009**, *4*, 839.
[6] C.-H. Liu, Y.-C. Chang, T. B. Norris, Z. Zhong, *Nat. Nanotechnol.* **2014**, *9*, 273.
[7] N. O. Weiss, H. Zhou, L. Liao, Y. Liu, S. Jiang, Y. Huang, X. Duan, *Adv. Mater.* **2012**, *2*4, 5782.
[8] B. J. Kim, S.-K. Lee, M. S. Kang, J.-H. Ahn, J. H. Cho, *ACS Nano*, **2012**, *6*, 8646.
[9] R. R. Nair, P. Blake, A. N. Grigorenko, K. S. Novoselov, T. J. Booth, T. Stauber, N. M. R. Peres, A. K. Geim, *Science* **2008**, *320*, 1308.
[10] F. H. L. Koppens, T. Mueller, Ph. Avouris, A. C. Ferrari, M. S. Vitiello, M. Polini, *Nat. Nanotechnol.* **2014**, *9*, 780.
[11] O. L.-Sanchez, D. Lembke, M. Kayci, A. Radenovic, Andras Kis, *Nat. Nanotechnol.* **2013**, *8*, 497.
[12] H. Tan, Y. Fan, Y. Zhou, Q. Chen, W. Xu, J. H. Warner, *ACS Nano* **2016**, *10*, 7866.
[13] E. Zhang, P. Wang, Z. Li, H. Wang, C. Song, C. Huang, Z.-G. Chen, L. Yang, K. Zhang, S. Lu, W. Wang, S. Liu, H. Fang, X. Zhou, H. Yan, J. Zou, X. Wan, P. Zhou, W. Hu, F. Xiu, *ACS Nano*, **2016**, *10*, 8067.
[14] Y.-H Chang, W. Zhang, Y. Zhu, Y. Han, J. Pu, J.-K. Chang, W.-T. Hsu, J.-K. Huang, C.-L. Hsu, M.-H. Chiu, T. Takenobu, H. Li, C.-I Wu, W.-H. Chang, A. T. S. Wee, L.-J. Li, *ACS Nano*, **2016**, *10*, 8067.
[15] C. Yan, C. Gong, P. Wangyang, J. Chu, K. Hu, C. Li, X. Wang, X. Du, T. Zhai, Y. Li, J. Xiong, *Adv. Funct. Mater.* **2018**, *2*8, 1803305.
[16] S. R. Tamalampudi, Y.-Y. Lu, R. Kumar U, R. Sankar, C.-D. Liao, K. Moorthy B, C.-H. Cheng, F. C. Chou, Y.-T. Chen, *Nano Lett.* **2014**, *14*, 2800.
[17] H. Liu, J. Meng, X. Zhang, Y. Chen, Z. Yin, D. Wang, Y. Wang, J. You, M. Gao, P. Jin, *Nanoscale* **2018**, *10*, 5559.
[18] X. Chen, X. Lu, B. Deng, O. Sinai, Y. Shao, C. Li, S. Yuan, V. Tran, K. Watanabe, T. Taniguchi, D. Naveh, L. Yang, F. Xia, *Nat. Commun.* **2017**, *8*, 1672.
[19] K. Xu, Y. Huang, B. Chen, Y. Xia. W. Lei, Z. Wang, Q. Wang, F. Wang, L. Yin, J. He, *Small* **2016**, *12*, 3106.
[20] K. E. Aretouli, P. Tsipas, D. Tsoutsou, J. M.-Velasco, E. Xenogiannopoulou, S. A. Giamini, E. Vassalou, N. Kelaidis, A. Dimoulas, *Appl Phys Lett*, **2015**, *106*, 143105.
[21] K. Xu, Z. Wang, F. Wang, Y. Huang, F.Wang, Y. Huang, L. Yin, C. Jiang, J. He, *Adv. Mater.* **2015**, *27*, 7881.
[22] D. Wang, J. Meng, X. Zhang, G. Guo, Z. Yin, H. Liu, L. Cheng, M. Gao, J. You, R. Wang, *Chem. Mater.* **2018**, *30*, 3819.
[23] L. Yin, K. Xu, Y. Wen, Z. Wang, Y. Huang, F. Wang, T. A. Shifa, R. Cheng, H. Ma, J. He *Appl Phys Lett*, **2016**, *109*, 213105.
[24] M. Kang, S. Rathi, I. Lee, L. Li, M. A. Khan, D. Lim, Y. Lee, J. Park, S. J. Yun, D.-H. Youn, C. Jun, G.-H. Kim, *Nanoscale* **2017**, *9*, 1645.

[25] C. Yan, L. Gan, X. Zhou, J. Guo, W. Huang, J. Huang, B. Jin, J. Xiong, T. Zhai, Y. Li, *Adv. Funct. Mater.* **2017**, *27*, 1702918.
[26] L. Li, W. Wang, L. Gan, N. Zhou, X. Zhu, Q. Zhang, H. Li, M. Tian, T. Zhai, *Adv. Funct. Mater.* **2016**, *26*, 8281.
[27] P. Perumal, R. K. Ulaganathan, R. Sankar, Y.-M. Liao, T.-M. Sun, M.-W. Chu, F. C. Chou, Y.-T. Chen, M.-H. Shih, Y.-F. Chen, *Adv. Funct. Mater.* **2016**, *26*, 3630.
[28] D. Wang, X. Zhang, G. Guo, S. Gao, X. Li, J. Meng, Z. Yin, H. Liu, M. Gao, L. Cheng, J. You, R. Wang, *Adv. Mater.* **2018**, *30*, 1803285.
[29] A. Ubaldini, J. Jacimovic, N. Ubrig, E. Giannini, *Cryst. Growth Des.* **2013**, *13*, 4453.
[30] M. Binnewies, R. Glaum, M. Schmidt, P. Schmidt, *Z. Anorg. Allg. Chem.* **2013**, *639*, 219.
[31] C. Gaiser, T. Zandt, A. Krapf, R. Serverin, C. Janowitz, R. Manzke, *Phys. Rev. B* **2004**, *69*, 075205.
[32] W. Ouyang, F. Teng, J.-H. He, X. Fang, *Adv. Funct. Mater.* **2019**, 1807672.
[33] M. Buscema, J. O. Island, D. J. Groenendijk, S. I. Blanter, G. A. Steele, H. S. J. van der Zant, A. C.-Gomez, *Chem. Soc. Rev.* **2015**, *44*, 3691.
[34] C.-H. Yeh, H.-C. Chen, H.-C. Lin,Y.-C. Lin, Z.-Y. Liang, M.-Y. Chou, K. Suenaga, P.-W. Chiu, *ACS Nano* **2019**, *13*, 3269.
[35] N. Huo, G. Konstantatos, *Adv. Mater.* **2018**, *30*, 1801164.
[36] R. B. J. Gedrim, M. Shanmugam, N. Jain, C. A. Durcan, M. T. Murphy, T. M. Murray, R. J. Matyi, R. L. Moore, B. Yu, *ACS Nano,* **2014**, *8*, 514.
[37] P. Hu, L. Wang, M. Yoon, J. Zhang, W. Feng, X. Wang, Z. Wen, J. C. Idrobo, Y. Miyamoto, D. B. Geohegan , K. Xiao, *Nano Lett.* **2013**, *13*, 1649.
[38] G. Su, V. G. Hadjiev, P. E. Loya, J. Zhang, S. Lei, S. Maharjan, P. Dong, P. M. Ajayan, J. Lou, H. Peng, *Nano Lett.* **2015**, *15*, 506.
[39] X. Gong, M. Tong, Y. Xia, W. Cai, J. S. Moon, Y. Cao, G. Yu, C.-L. Shieh, B. Nilsson, A. J. Heeger, *Science*, **2009**, *325*, 1665.
[40] Z. Sun, H. Chang, *ACS Nano* **2014**, *8*, 4133.
[41] R. K. Ulaganathan, Y.-Y. Lu, C.-J. Kuo, S. R. Tamalampudi, R. Sankar, K. M. Boopathi, A. Anand, K. Yadav, R. J. Mathew, C.-R. Liu, F. C. Chou,Y.-T. Chen, *Nanoscale* **2016**, *8*, 2284.
[42] G. Konstantatos, M. Badioli, L. Gaudreau, J. Osmond, M. Bernechea, F. P. G. de Arquer, F. Gatti and F. H. L. Koppens, *Nat. Nanotechnol.* **2012**, *7*, 363.
[43] X. Li, J. E. Carey, J. W. Sickler, M. U. Pralle, C. Palsule and C. J. Vineis, *Opt. Express* **2012**, *20*, 5518.
[44] A. Zhang, H. Kim, J. Cheng, Y.-H. Lo, *Nano Lett.* **2010**, *10*, 2117.
[45] L. Cao, J.-S. Park, P. Fan, B. Clemens, M. L. Brongersma, *Nano Lett.* **2010**, *10*, 1229.
[46] C. L. Tsai, K. Y. Cheng, *Appl. Phys. Lett.* **2007**, *91*, 181105.
[47] W. Deng, Y. Chen, C. You, B. An, B. Liu, S. Li, Y. Zhang, H. Yan, L. Sun, *2D Mater.* **2018**, *5*, 045027.
[48] H. J. Conley, B. Wang, J. I. Ziegler, R. F. Haglund Jr, S. T. Pantelides, K. I. Bolotin, *Nano Lett.* **2013**, *13*, 3626.
[49] G.-H. Lee, Y.-J. Yu, X. Cui, N. Petrone, C.-H. Lee, M. S. Choi, D.-Y. Lee, C. Lee, W. J. Yoo, K. Watanabe, T. Taniguchi, C. Nuckolls, P. Kim, J. Hone, *ACS Nano* **201**3, *7*, 7931.

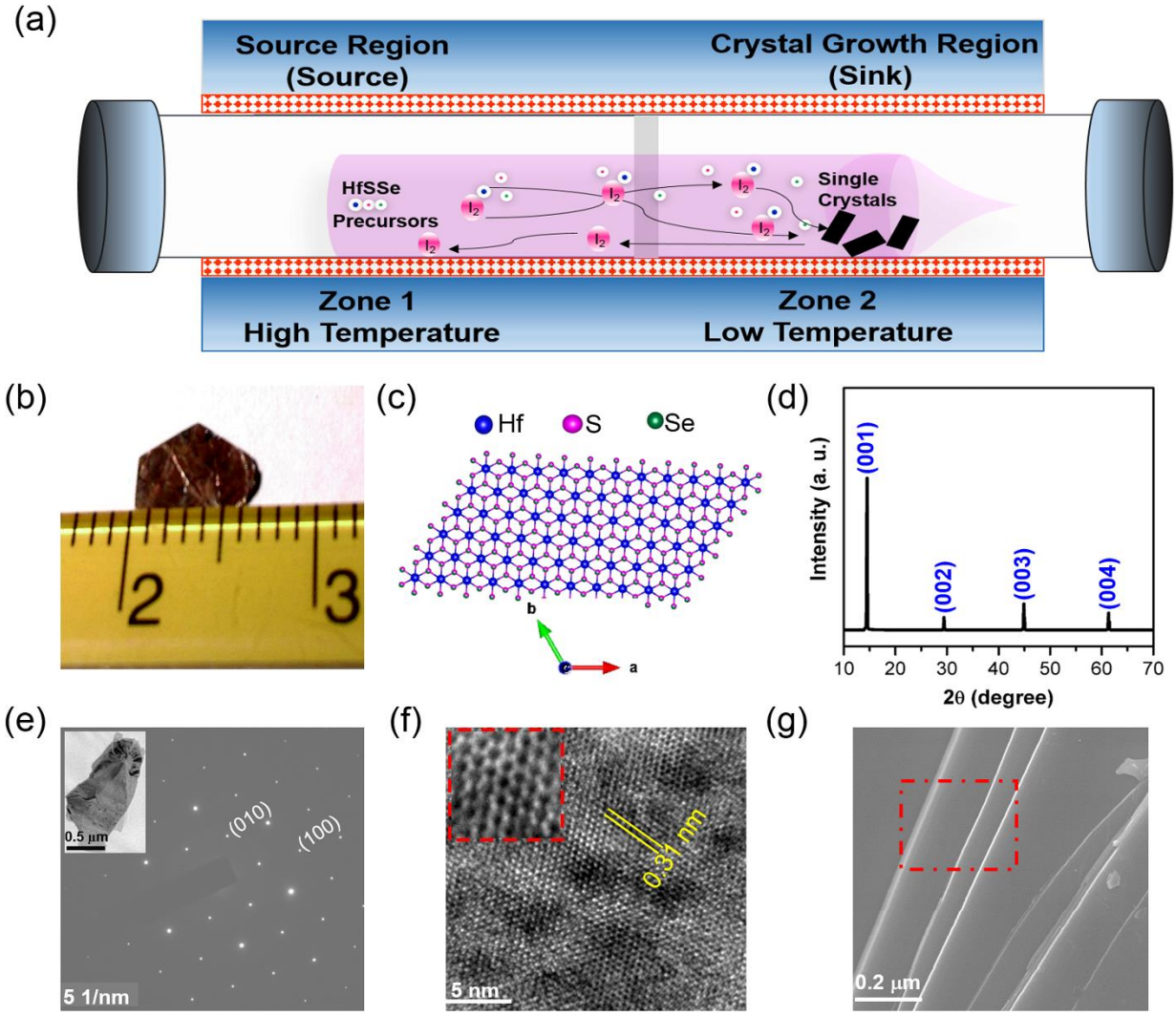

Figure 1. (a) Schematic diagram for CVT method single crystal growth of HSS. (b) Optical image of the as-grown HSS single crystal. (c) Top view of the crystal structure of HSS. (d) XRD diffraction pattern of the as-grown HSS single crystal along the c-direction of preferred orientation. (e) The SAED pattern of HSS crystal, inset shows TEM image of cleaved few-layered HSS flakes, and the corresponding (f) real space view of HSS crystal image through Fourier transform shows a clear hexagonal symmetry with a magnified view in the inset. (g) With the FE-SEM image, clear layered nature is identified for the freshly cleaved HSS single crystal.

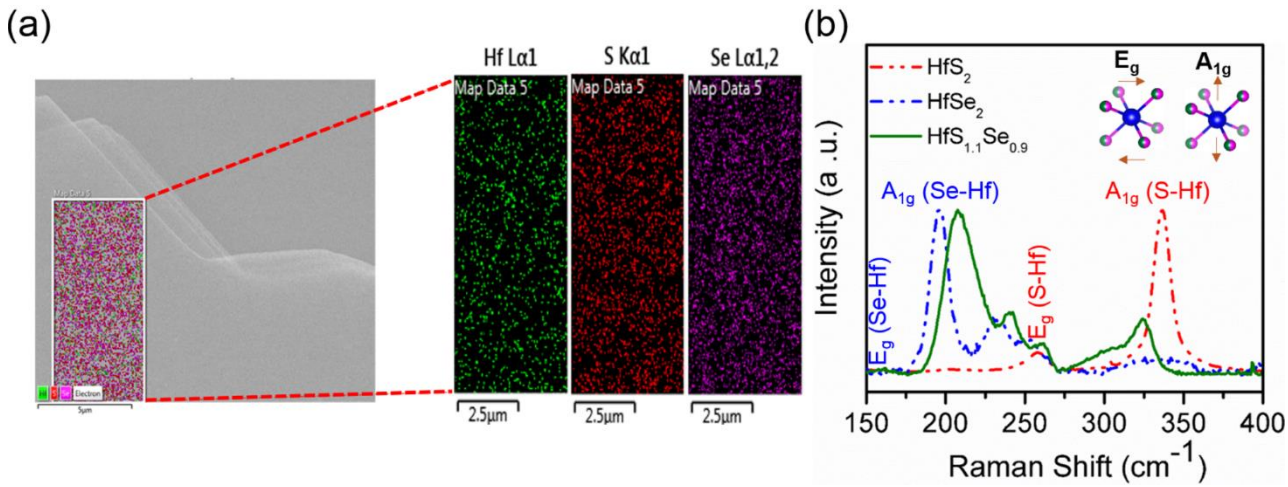

Figure 2. (a) The elemental analysis of the as-grown HSS single crystal, where S and Se mappings display homogeneity at the micron size level. (b) Raman spectra of the HSS flakes measured under ambient conditions with laser excitation at 488 nm. The phonon modes of HSS crystal are compared with the indexed A_{1g} and E_g modes for the pure HfS_2 and $HfSe_2$.

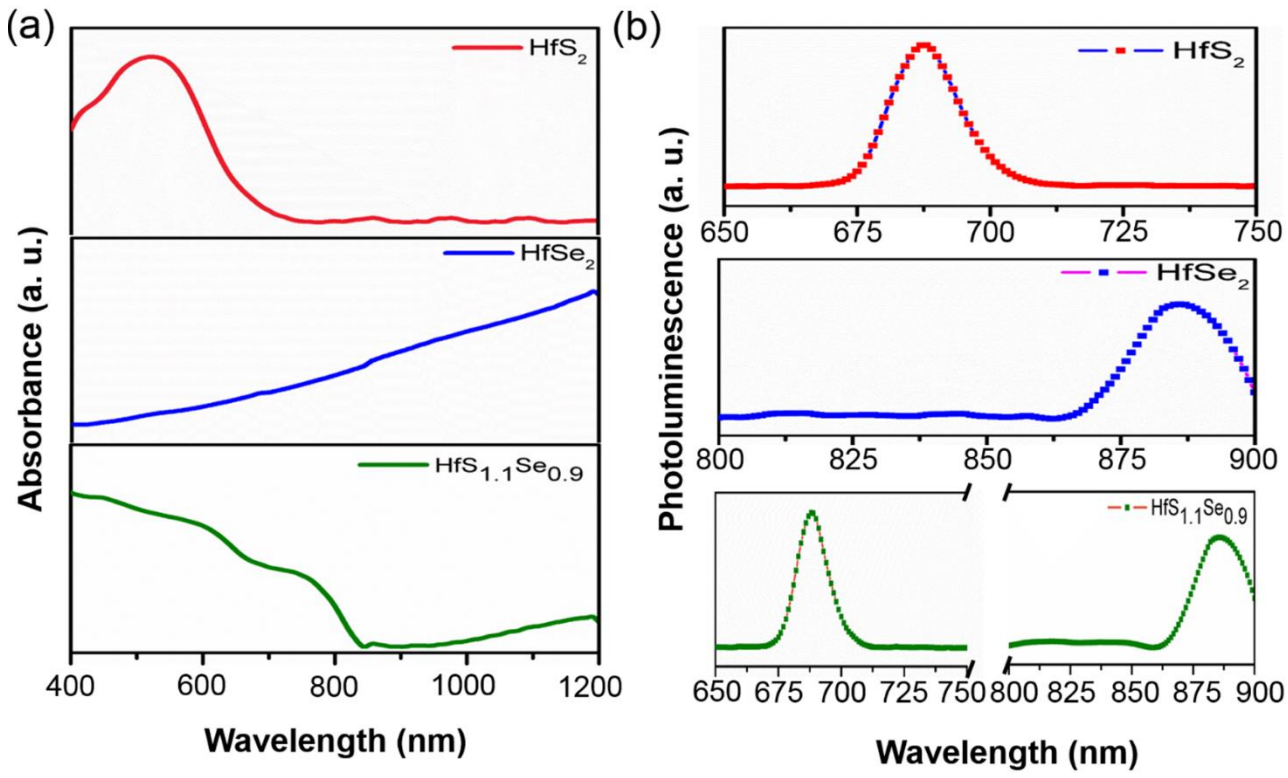

Figure 3. (a) Absorption spectrum of the as-grown $HfS_{1.1}S_{0.9}$ crystal is compared with those of the pristine HfS_2 and $HfSe_2$. (b) Photoluminescence of $HfS_{1.1}S_{0.9}$ shows an emission spectrum at 688 nm and 886 nm, which overlaps with the emission peaks of HfS_2 and $HfSe_2$.

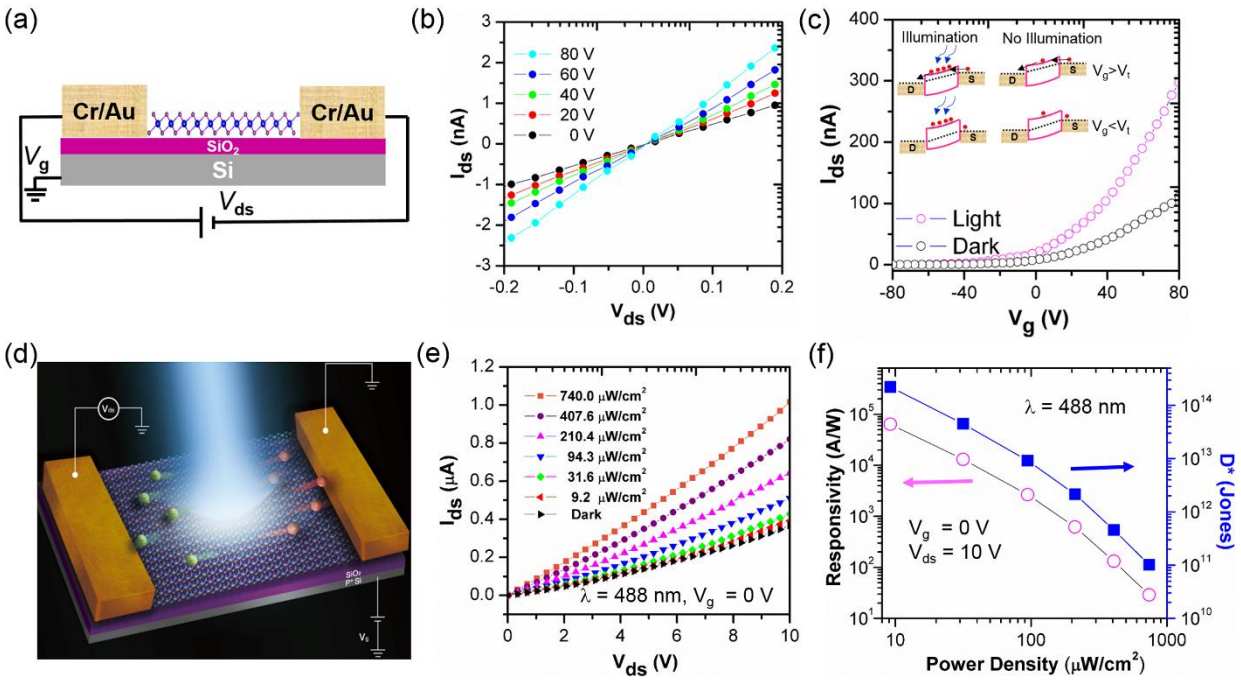

Figure 4. Characteristics of HSS phototransistor prepared on a rigid substrate of SiO_2/Si. (a) The diagrammatic sketch of HSS-FET. (b) Output characteristics of few-layered HSS-FET under different gate voltages from 0 to 80 V in +20 V/step. (c) Transfer characteristics of HSS-FET under dark and white light illumination. Inset shows the band bending diagram under illumination and no illumination with above and below the threshold voltage. (d) The schematic illustration of few-layered HSS under optoelectronic investigation with a laser source. (e) I_{ds}-Vds curve of HSS photodetector in dark and different power of 488 nm laser irradiation. (f) Responsivity and specific detectivity vs power density at 10V of V_{ds} and V_g of 0V.

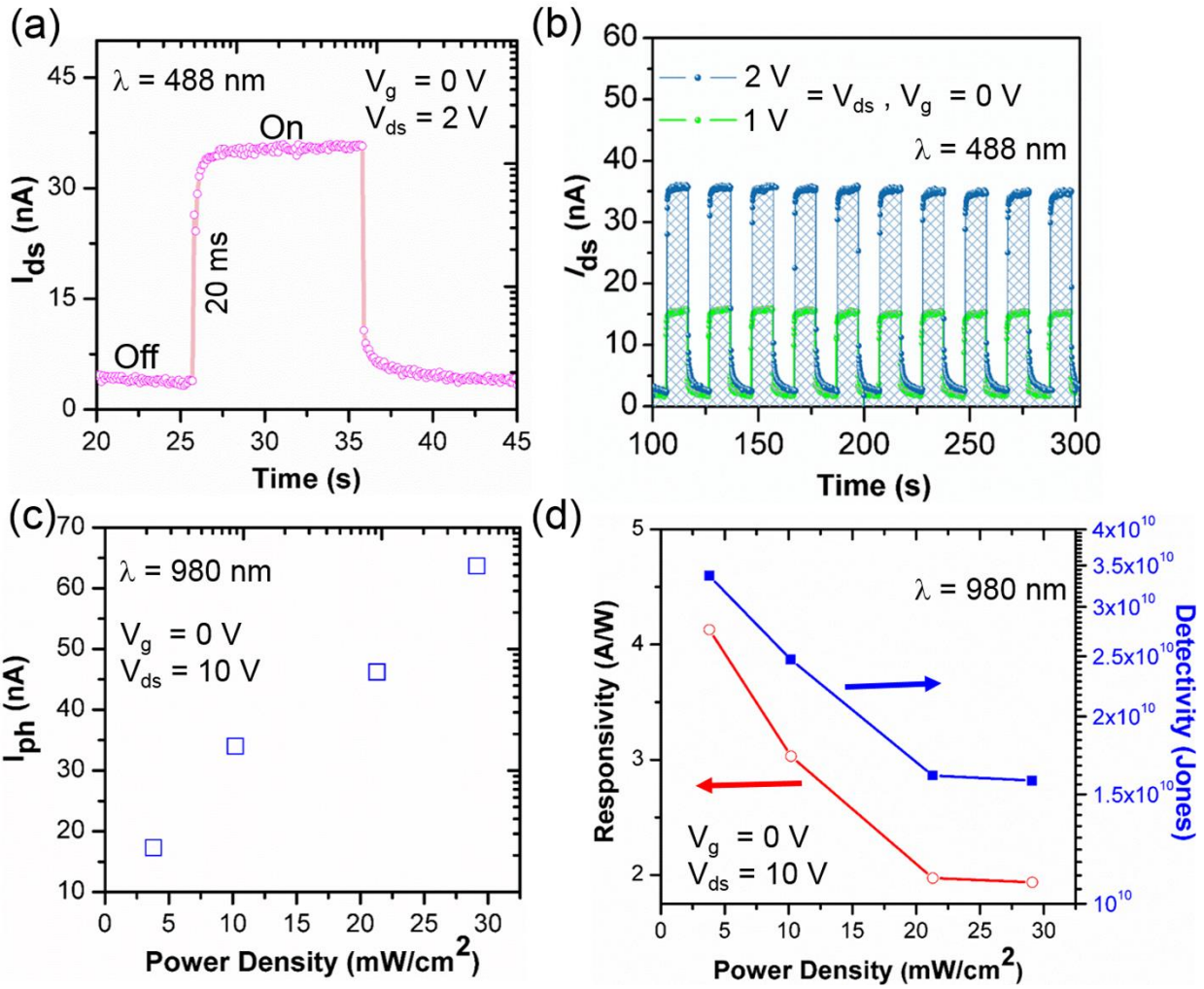

Figure 5. (a)Time-resolved photoresponse of few-layered HSS. (b) Photo switching stability HSS photodetector was examined at various V_{ds} = (1,2), respectively. (c) Infrared-photodetector of few-layered HSS. The Photocurrent (I_{ph}) is plotted as a function of incident laser power. (d) The Responsivity and calculated Detectivity of the HSS were acquired as a function of different incident power of 980 nm.

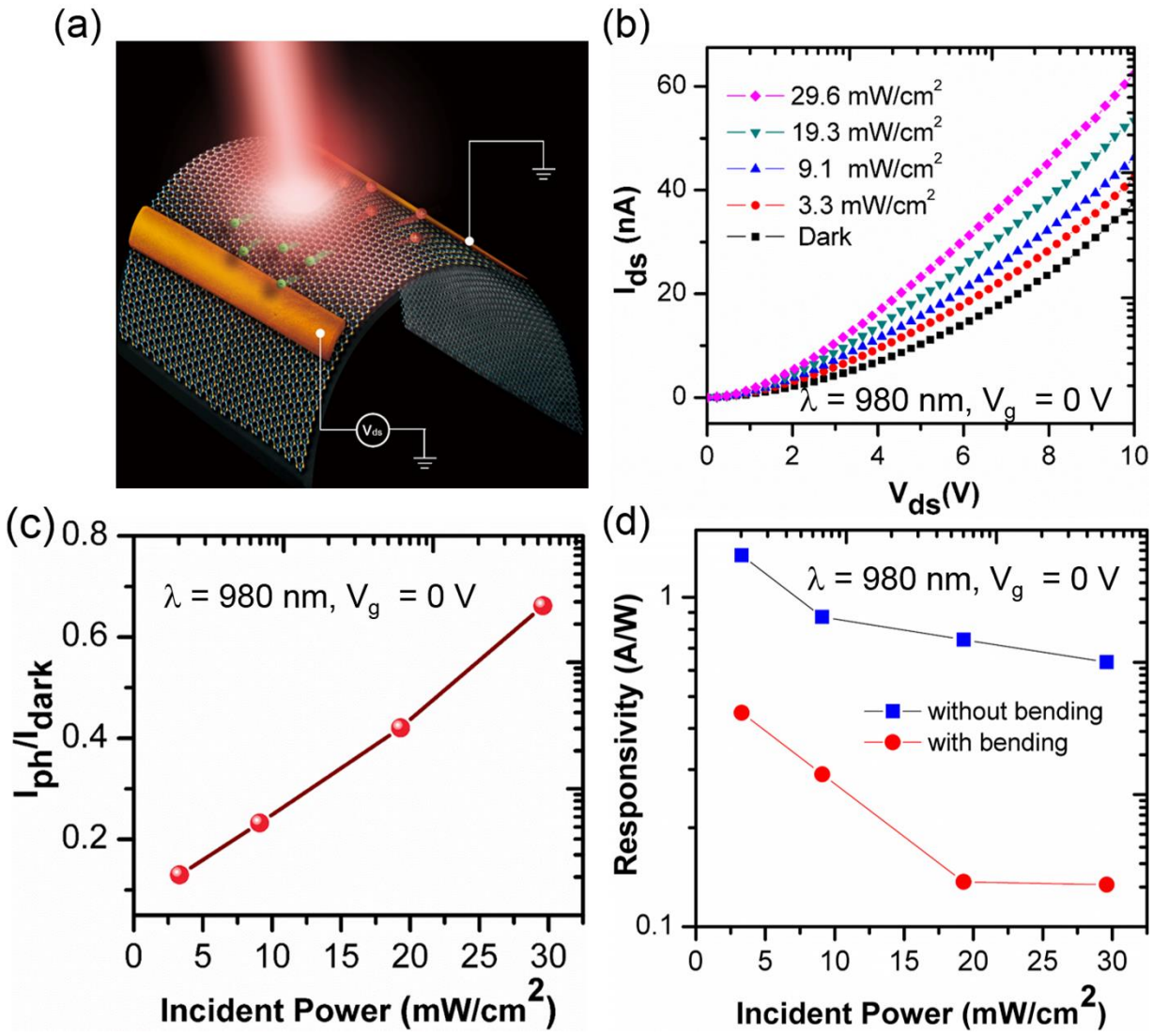

Figure 6. The photodetector of HSS on a flexible PET substrate under 980 nm. (a) Schematic plot of the HSS-FET on a flexible substrate under near-infrared illumination. (b) I_{ds} vs V_{ds} curve under 980 nm irradiation of various power. (c) Photosensitivity (I_{ph}/I_{dark}) measured as a function of incident power density. (d) Responsivity vs. power density under bent with unbent conditions.

High-performance Flexible Broadband Photodetectors Based on 2D Hafnium Selenosulfide Nanosheets

Rajesh Kumar Ulaganathan, Raman Sankar, Chang-Yu Lin*, Raghavan Chinnambedu Murugesan, Kechao Tang, and Fang-Cheng Chou**

Dr. R. K. Ulaganathan, Prof. R. Sankar, Prof. F. C. Chou
Center for Condensed Matter Sciences
National Taiwan University
Taipei 10617, Taiwan
sankarraman@phys.sinica.edu.tw, fcchou@ntu.edu.tw

Prof. C.-Y Lin
Department of Mechanical Engineering
Chung Yuan Christian University
Taoyuan 32023, Taiwan
cylin@cycu.edu.tw

Prof. C.-Y Lin, Dr. K. Tang
Department of Materials Science and Engineering,
University of California, Berkeley, 94720, USA

Prof. C.-Y Lin, Dr. K. Tang,
Lawrence Berkeley National Laboratory
Materials Sciences Division
Berkeley, USA

Dr. R. C. Murugesan
Aston Institute of Photonic Technologies
Aston University
Birmingham, B4 7ET, UK

Prof. R. Sankar
Institute of Physics
Academia Sinica
Taipei 11529, Taiwan

Prof. F. C. Chou
Taiwan Consortium of Emergent Crystalline Materials
Ministry of Science and Technology
Taipei 10622, Taiwan

Prof. F. C. Chou
Center of Atomic Initiative for New Materials
National Taiwan University
Taipei 10617, Taiwan

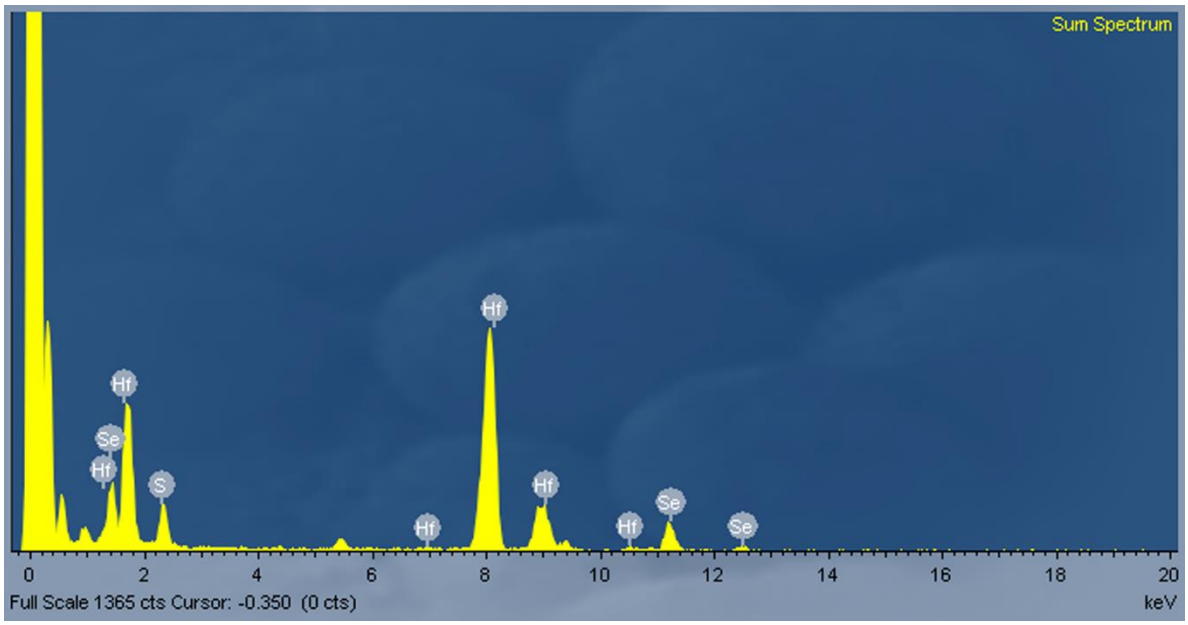

Figure S1. EDX spectrum the bulk HSS.

Table S1. The electron probe micro-analysis (EPMA) of Hf, S and Se atoms.

Sample Positions	**Hf**	**S**	**Se**	**Total**
	Atomic %			
1	33.629	37.8711	28.4999	100
2	33.8189	37.3644	28.8167	100
3	33.7843	37.4739	28.7418	100
4	33.9612	37.6044	28.4343	100
5	34.0736	37.2592	28.6672	100
Average	33.8534	37.5146	28.63198	100

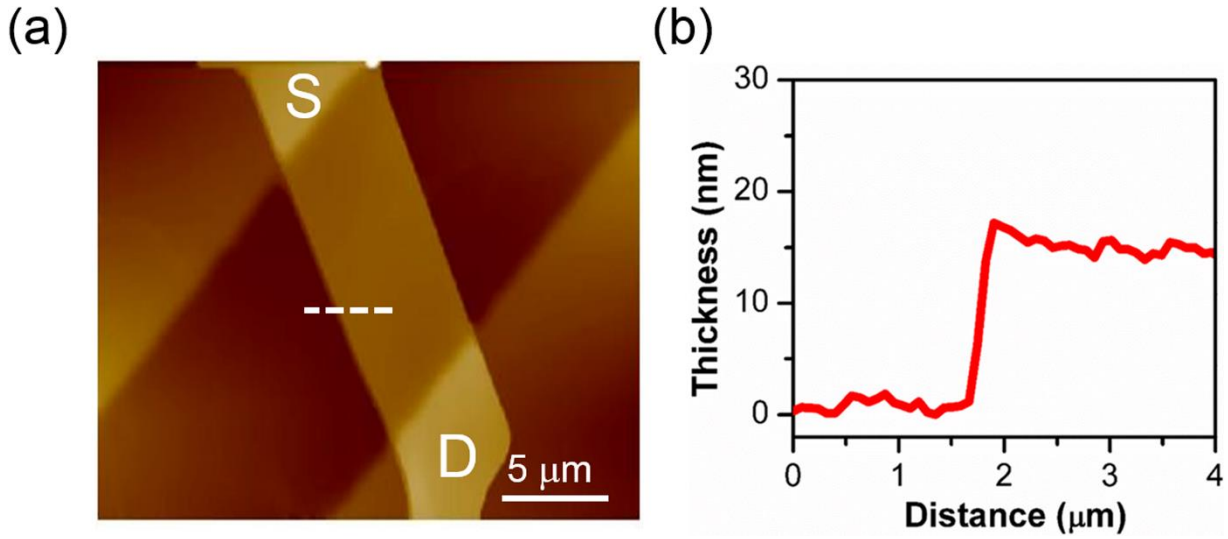

Figure S2. (a) AFM surface topography of the as-fabricated HSS-FET, S and D in the image represents source and drain electrode. (b) The thickness of the HSS nanosheets is measured ~15 nm in height.

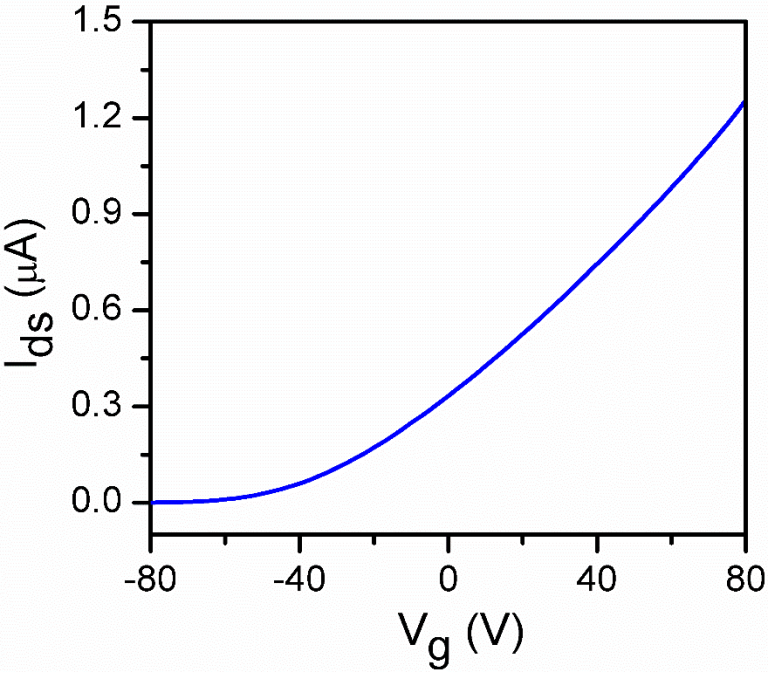

Figure S3. I_{ds}-V_g characteristic curve measured at V_g from -80 V to 80 V at V_{ds} = 1 V.

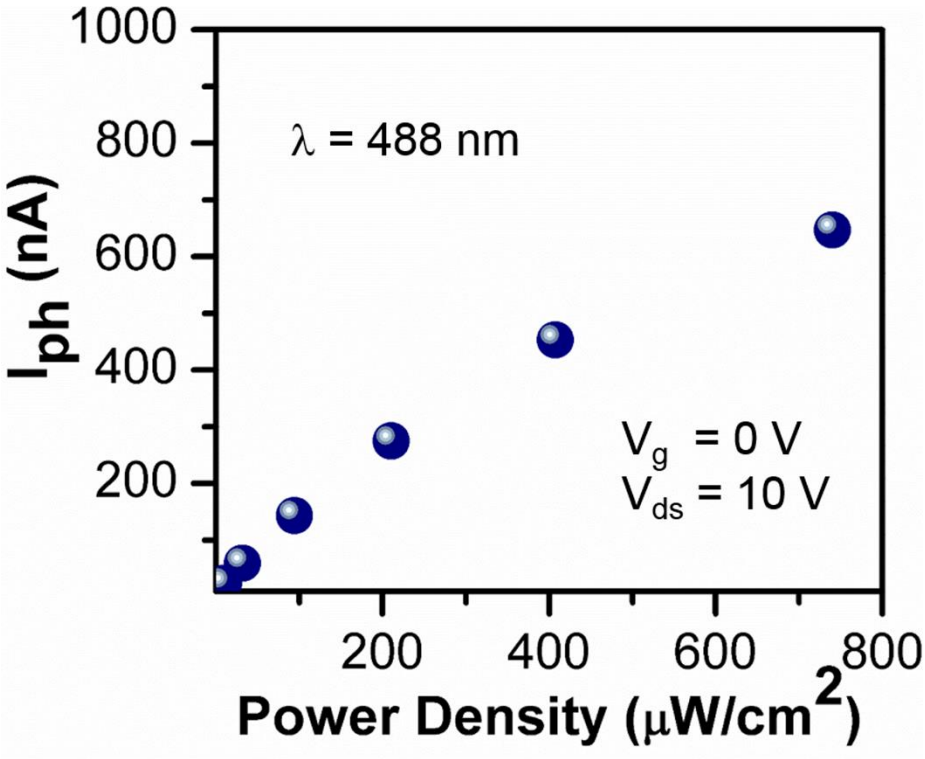

Figure S4. The photocurrent (I_{ph}) is plotted as a function of the laser power (P) measured at V_{ds} = 10 V and V_g = 0 V; the data points (blue circle) were collected from (Figure 4e).

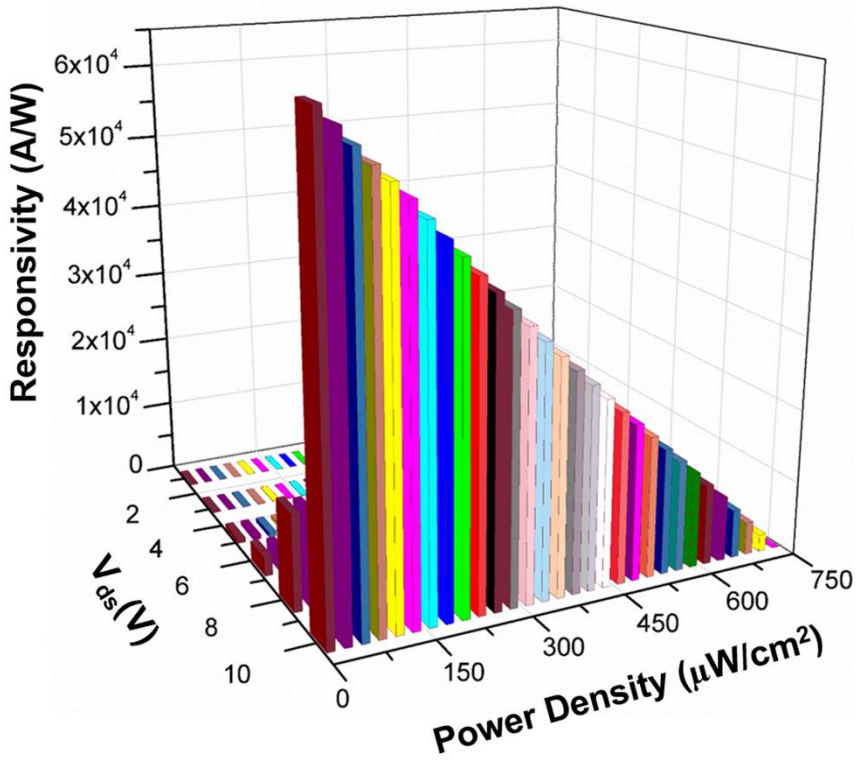

Figure S5. 3D matrix chart of responsivity with respect to power density and V_{ds}.

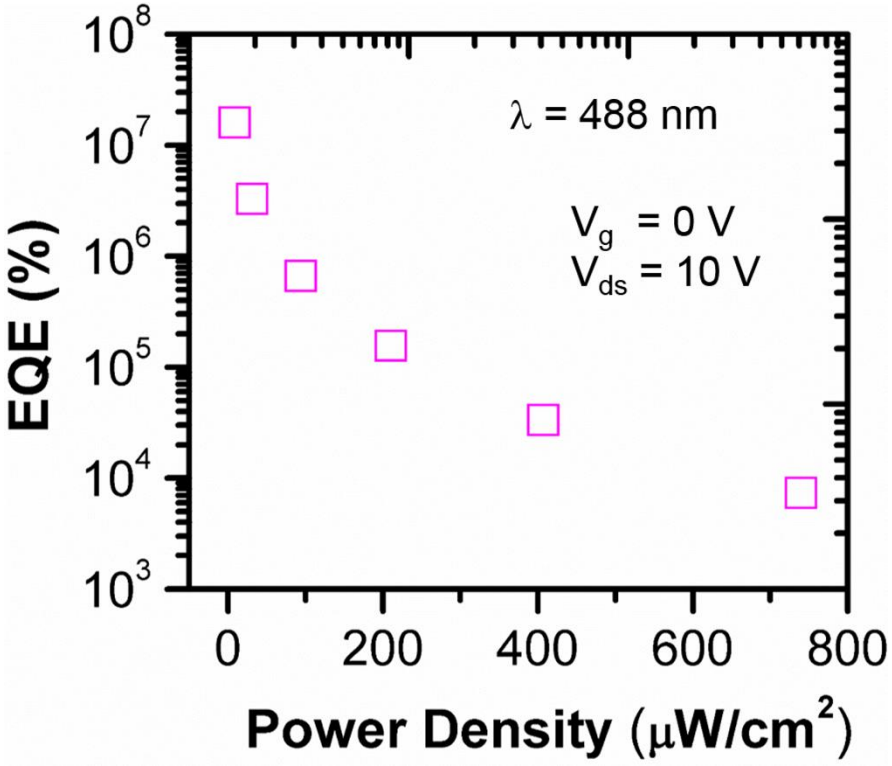

Figure S6. The EQE of the few-layered HSS photodetector as a function of different excitation power at V_g = 0 V, and V_{ds} = 10 V.

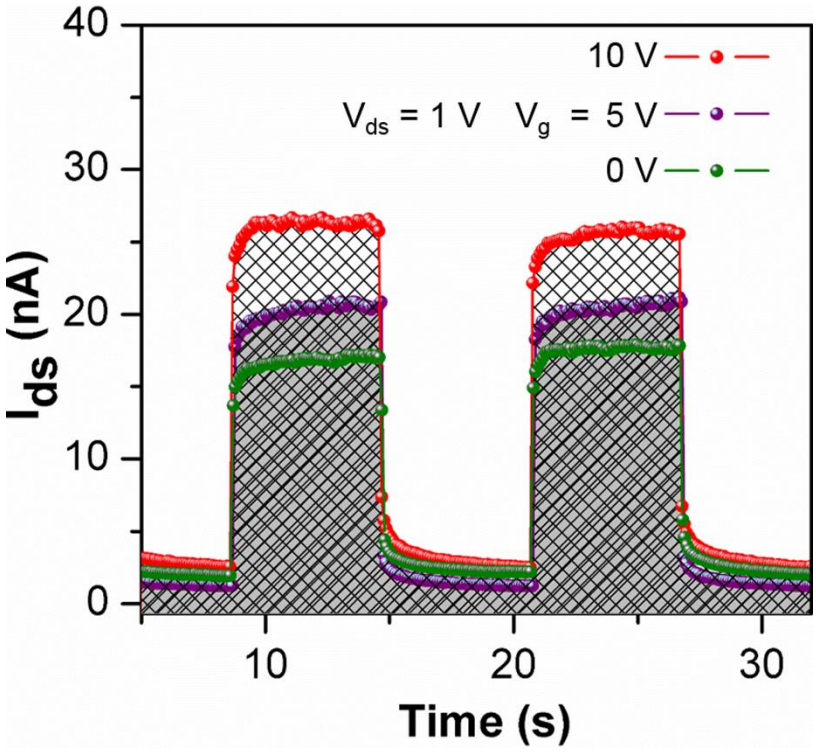

Figure S7. Time-resolved photoresponse of the HSS photodetector was examined at various V_g (= 0, 5, 10 V) with constant V_{ds} of 1 V.

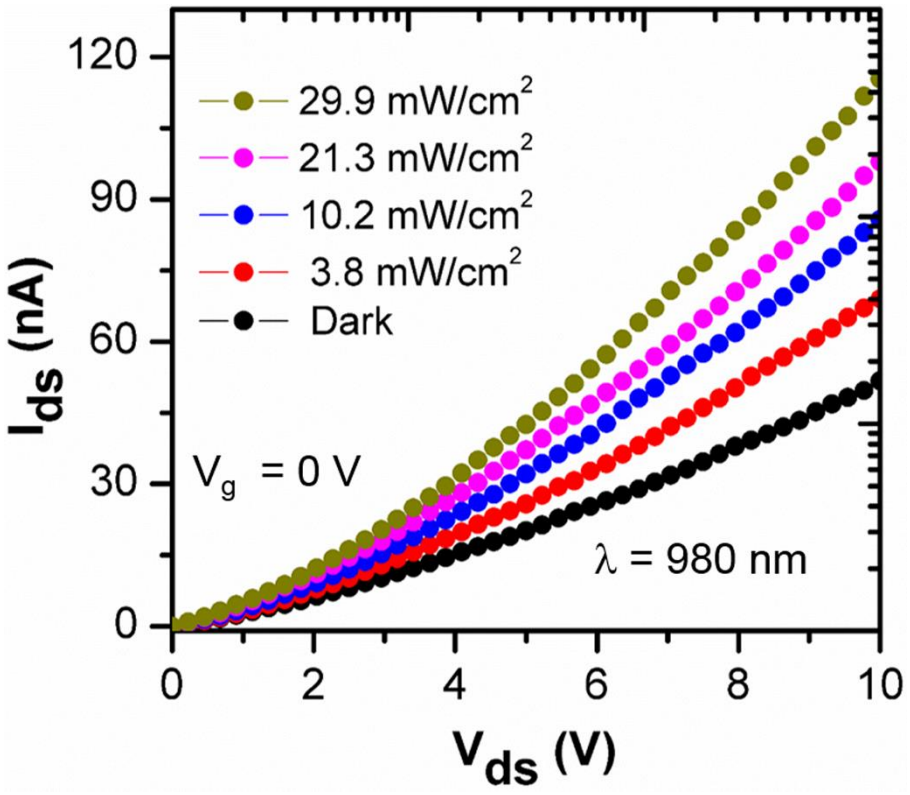

Figure S8. The I_{ds}–V_{ds} curves of a HSS-FET at Vg = 0 V with 980 nm excitation at laser powers of 3.8, 10.2, 21.3, and 29.9 mW/cm^2.

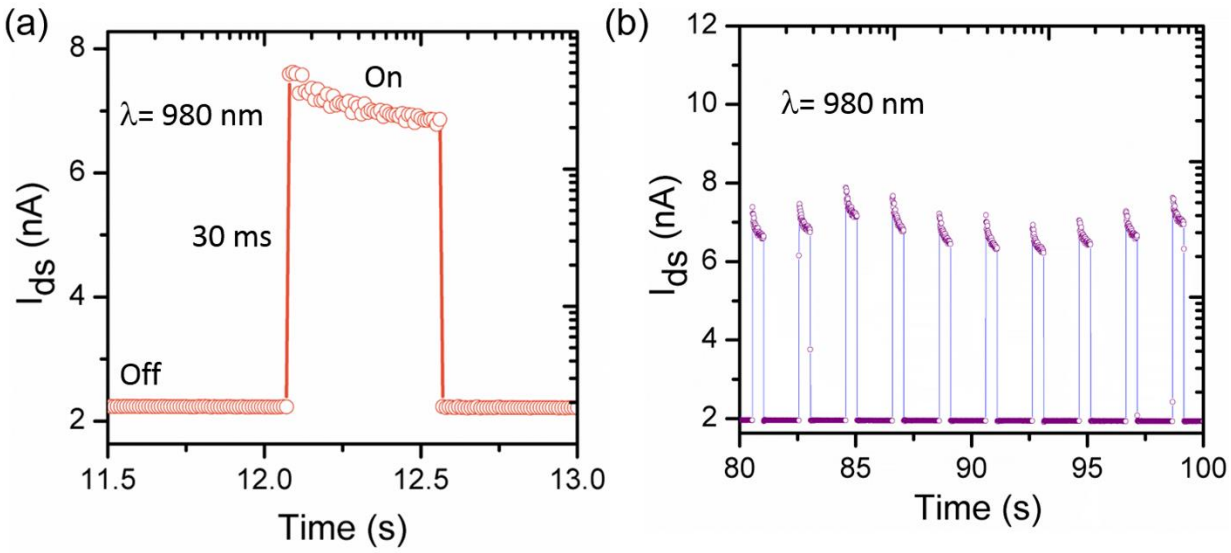

Figure S9. (a)Time-resolved photoresponse of HSS-FET under 980 nm laser. (b) Switching stability of HSS phototransistors under $V_g = 0$ V and $V_{ds} = 1$V.

Table S2. Summary of performance metrics of the Hf-chalcogenides based 2D photodetectors

Material	Fabrication Method	Measurement Conditions	Responsivity (A/W)	Response Time	Detectivity (Jones)	References
HfS_2	CVD	450 nm V_{ds} = 10 V V_g = 0 V	$0.01*10^{-3}$	130 µS	10^8	S1
HfS_2	CVD	520 nm V_{ds} = 5 V	$2.8*10^{-3}$	55 ms	-	S2
HfS_2	Mechanical Exfoliation	473 nm V_{ds} = 3 V V_g = 80 V	890	38 ms	10^{10}	S3
$HfSe_2$	Mechanical Exfoliation	520 nm V_{ds} = 0.1 V V_g = -60 V	26.44	-	-	S4
$HfSe_2$	Mechanical Exfoliation	473 nm V_{gs} = 80 V	252	180 ms	$3*10^{11}$	S5
HfS_2/h-BN	CVD	450 nm V_{ds} = 10 V	0.026	200 µS	$3*10^{11}$	S6
$HfS_{2(1-x)}Se_{2x}$ Alloy	CVD	450 nm V_{ds} = 10 V	0.11	190 µS	10^{12}	S7
HSS Single Crystal	CVT-Mechanical Exfoliation	488 nm V_{ds} = 10 V V_g = 0 V	$\sim 6.4\times10^4$	20 ms	10^{14}	This Work
		980 nm V_{ds} = 10 V V_g = 0 V	4.2		$3.36*10^{10}$	

References

[S1] D. Wang, X. Zhang, H. Liu, J. Meng, J. Xia, Z. Yin, Y. Wang, J. You, X.-M. Meng, *2D Mater*. **2017**, *4*, 031012.

[S2] C. Yan, L. Gan, X. Zhou, J. Guo, W. Huang, J. Huang, B. Jin, J. Xiong, T. Zhai, Y. Li, *Adv. Mater*. **2017**, *27*, 1702918.

[S3] K. Xu, Z. Wang, F. Wang, Y. Huang, F.Wang, Y. Huang, L. Yin, C. Jiang, J. He, *Adv. Mater.* **2015**, *27*, 7881.

[S4] M. Kang, S. Rathi, I. Lee, L. Li, M. A. Khan, D. Lim, Y. Lee, J. Park, S. J. Yun, D.-H. Youn, C. Jun, G.-H. Kim, *Nanoscale* **2017**, *9*, 1645.

[S5] L. Yin, K. Xu, Y. Wen, Z. Wang, Y. Huang, F. Wang, T. A. Shifa, R. Cheng, H. Ma, J. He *Appl Phys Lett*, **2016**, *109*, 213105.

[S6] D. Wang, J. Meng, X. Zhang, G. Guo, Z. Yin, H. Liu, L. Cheng, M. Gao, J. You, R. Wang, *Chem. Mater*. **2018**, *30*, 3819.

[S7] D. Wang, X. Zhang, G. Guo, S. Gao, X. Li, J. Meng, Z. Yin, H. Liu, M. Gao, L. Cheng, J. You, R. Wang, *Adv. Mater.* **2018**, *30*, 1803285.